

**Studies of DPPA & LPS Monolayers on Aqueous Solutions by
Surface Tensiometry and Brewster Angle Microscopy**

THESIS

Presented in Partial Fulfillment of the Requirements for the Degree Master of Science
in the Graduate School of The Ohio State University

By

Ting Zhang, B.S.

Graduate Program in Chemistry

The Ohio State University

2014

Master's Examination Committee:

Prof. Dr. Heather C. Allen, Advisor

Prof. Dr. Terry L. Gustafson

Copyright by

Ting Zhang

2014

Abstract

In this work, surface pressure-area isotherms and Brewster angle microscopy (BAM) images were obtained for Langmuir monolayers of dipalmitoyl-phosphatidic acid (DPPA) on neat water and aqueous solutions of NaCl, KCl, MgCl₂, CaCl₂, and Gibbs monolayers of bacterial lipopolysaccharide (LPS). Monolayers of DPPA and LPS on water serve as representative model systems for organic surfactants on the surface of marine aerosols due to their important biological functions.

BAM images of DPPA reveal that condensed monolayers form even at low surface pressures and quickly merge into homogeneous continuous films. Surface pressure-area isotherms of DPPA monolayers reveal a tight packing due to strong hydrogen bonding interactions, with slight expansion of the monolayers upon the addition of Na⁺, K⁺, Mg²⁺, and Ca²⁺. These cations were found to expand the monolayer to different degrees dependent on their chemical nature. The ability of DPPA to pack tightly in homogeneous films has important implications in aerosol properties.

LPS was found to form soluble monolayers and diffuse easily into the bulk. However it becomes more surface active in the presence of Na⁺, a common ocean cation. This implicates LPS as an important surface-active molecule on the surface of marine aerosols, which contain salt cores surrounded by an organic coating.

Dedication

This thesis is dedicated to science.

Acknowledgements

First and foremost, I acknowledge my advisor, Dr. Heather C. Allen, for her support, encouragement and advice through this project. I would also like to thank Dr. Dominique Verreault for invaluable advice providing feedback on results and help in proofreading this thesis. Without the help and guidance of Dr. Dana M. Telesford, and Ellen C. Adams, I would not understand Langmuir trough and BAM as well as I do.

Vita

February 9th, 1991 Born – Stuttgart, Germany

May 2012..... B.S. Chemistry, College of William & Mary,
Williamsburg, VA, USA

September 2012 – Present..... Graduate Teaching Associate, Department
of Chemistry and Biochemistry, The Ohio
State University – Columbus, Ohio, USA

Publications

Hogg, D.; Alfeeli, B.; Hoover, A.; Zhang T.; Rice, G.; Agah, M., "Trace organics monitoring in drinking water using Tenax-coated fibers," *Sensors, 2011 IEEE, 2011*, 1093-1096.

Field of Study

Major Field: Chemistry

Table of Contents

Abstract	ii
Dedication	iii
Acknowledgements	iv
Vita	v
Publications	v
Field of Study	v
Table of Contents	vi
List of Figures	x
List of Tables	xiii
List of Abbreviations and Symbols	xiv
Introduction	1
1.1 Overview	1
1.2 Motivations	3
1.2.1 Aerosols on Climate	3
1.2.2 Marine Aerosols and the SSML	6
1.2.3 Ion Relevance in Marine Aerosols	7
1.2.4 DPPA and LPS Relevance	8

1.2.5 Mixing and Complexity	9
1.3 Surfactants.....	10
1.3.1 Phospholipids.....	10
1.3.2 DPPA	13
1.3.3 LPS.....	14
1.4 Objectives	16
Chapter 2: Theory and Instrumentation	17
2.1 Surface Tensiometry	17
2.1.1 Gibbs Adsorption Equation.....	17
2.1.2 Surface Free Energy and Surface Tension.....	20
2.1.3 Method of Measuring Surface Tension.....	22
2.1.4 Langmuir and Gibbs Monolayers.	25
2.1.5 Isotherms and Phases	26
2.2 Brewster Angle Microscopy	29
2.2.1 Plane Harmonic Waves.....	30
2.2.2 Polarization States.....	31
2.2.3 Reflection and Refraction	32
2.2.4 Brewster Angle	35
2.2.5 Factors for Intensity of Light.....	36
Chapter 3: Material and Methods	37

3.1 Materials	37
3.2 Methods.....	37
3.2.1 Sample Preparation	37
3.2.2 Π -A Isotherms	39
3.2.3 BAM Images	40
Chapter 4: Results and Discussion.....	42
4.1 Surface Pressure Isotherms	42
4.1.1 Phase behavior of DPPA on water.....	42
4.1.2 Effect of pH and ionization on the phase behavior of DPPA on water	44
4.1.3 Effect of monovalent cations on the phase behavior of DPPA.....	46
4.1.4 Effect of monovalent cations on the phase behavior of DPPA at low and high pH.....	53
4.1.5 Effect of divalent cations on the phase behavior of DPPA.....	55
4.1.6 Effect of surface-active contaminants on the phase behavior of DPPA	58
4.1.7 Phase behavior of DPPA on ASW.....	59
4.1.8 Comparison of salt effects on the phase behavior of DPPA	60
4.1.9 Phase behavior and surface propensity of LPS.....	62
4.2 BAM Images.....	63
4.2.1 Monolayer morphology of DPPA.....	63
Chapter 5: Conclusions and Future Work.....	78

References..... 81

List of Figures

Figure 1.1 Bar chart for radiative forcing (hatched) and effective radiative forcing (solid)	4
Figure 1.2 Schematic representation of direct and indirect cloud albedo effect.....	5
Figure 1.3 Representation of the SSML.....	6
Figure 1.4 Diagram of cell membrane	11
Figure 1.5 Structures of common membrane lipids.....	12
Figure 1.6 General structure of LPS	15
Figure 2.1 The interface between two bulk phases of real and ideal systems.	17
Figure 2.2 Schematic diagram of Langmuir trough with Wilhelmy plate open and closed.	22
Figure 2.3 Diagram of electromagnetic wave.....	30
Figure 2.4 Reflection and refraction of a plane-harmonic wave at an interface.....	32
Figure 4.1 Visual representation of law of matching water affinities.....	51
Figure 4.2 Visual representation of DPPA monolayer expansion on neat water, Ca ²⁺ , and Na ⁺ solutions.....	62
Figure 4.3 Π -A isotherm of DPPA monolayer on nanopure water	65
Figure 4.4 Literature Π -A isotherms of DPPA monolayers on water	65
Figure 4.5 Speciation curves of DPPA in water	66
Figure 4.6 Π -A isotherms of DPPA monolayers on nanopure water at various pH.....	66

Figure 4.7 Π -A isotherms of DPPA monolayers on NaCl solutions	67
Figure 4.8 Saturation curve of DPPA monolayers on NaCl solutions.....	67
Figure 4.9 Π -A isotherms of DPPA monolayers on KCl solutions	68
Figure 4.10 Π -A isotherms of DPPA monolayers on monovalent chloride salts	68
Figure 4.11 Π -A isotherms of DPPA monolayers on monovalent chloride salts at acidic pH.....	69
Figure 4.12 Π -A isotherms of DPPA monolayers on monovalent chloride salts at basic pH.....	69
Figure 4.13 Π -A isotherms of DPPA monolayers on MgCl ₂ solutions	70
Figure 4.14 Π -A isotherms of DPPA monolayers on CaCl ₂ solutions	70
Figure 4.15 Π -A isotherm of DPPA monolayer on divalent salts	71
Figure 4.16 Π -A isotherms of DPPA monolayers on all chloride salts.....	71
Figure 4.17 Π -A isotherms of DPPA monolayers on NaCl, baked and used as received.	72
Figure 4.18 Π -A isotherms of DPPA monolayers on MgCl ₂ , baked and used as received.	72
Figure 4.19 Π -A isotherms of DPPA monolayers on CaCl ₂ , baked and used as received.	73
Figure 4.20 Π -A isotherms of DPPA monolayers on chloride salts, and custom-made and commercial ASW	73
Figure 4.21 Π -A isotherm of phenol-purified LPS.....	74
Figure 4.22 Π -A isotherm of TCA-purified LPS.....	74

Figure 4.23 Relaxation curve of LPS. Experimental data (solid line) and viscoelastic fit (dashed line) are shown	75
Figure 4.24 BAM images of a DPPA monolayer on water during compression.....	75
Figure 4.25 BAM images of DPPA monolayer on NaCl solution during compression ..	76
Figure 4.26 BAM images of DPPA monolayer on KCl solution during compression....	76
Figure 4.27 BAM images of DPPA monolayer on MgCl ₂ solution during compression..	77
Figure 4.28 BAM images of DPPA monolayer on CaCl ₂ solution during compression .	77

List of Tables

Table 3.1 Chemical composition and ion concentration of Instant Ocean [®] synthetic sea salt	39
Table 4.1 Bare and hydrated ionic radii and their associated Gibbs free energy of hydration	49
Table 4.2 Bare and hydrated ionic radii and their associated Gibbs free energy of hydration	57

List of Abbreviations and Symbols

Abbreviations

ASW	artificial sea water
BAM	Brewster angle microscopy
CAICE	Center for Aerosol Impacts on Climate and the Environment
CCD	charge-coupled device
CDNC	cloud droplet number concentration
CSD	constrained sessile drop
DPPA	dipalmitoyl-phosphatidic acid
EDTA	ethylenediaminetetraacetic acid
EM	electromagnetic
G	gaseous
GDS	Gibbs dividing surface
HWP	half-wave plate
IPCC	Intergovernmental Panel on Climate Change
LC	liquid-condensed
LE	liquid-expanded
LPS	lipopolysaccharide
LWB	Langmuir-Wilhelmy balance
MMA	mean molecular area
PA	palmitic acid
PC	phosphatidylcholine
PD	pendant drop
PE	phosphatidylethanolamine
PI	phosphatidylinositol

PLA	phospholipase A
PLB	phospholipase B
PLC	phospholipase C
PLD	phospholipase D
POPC	1-palmitoyl-2-oleoylphosphatidylcholine
PS	phosphatidylserine
S	solid
SDS	sodium dodecyl sulfate
SP	surface pressure
SSML	sea surface microlayer
TC	tilted-condensed
TCA	trichloroacetic acid
UC	untilted-condensed
VSFG	vibrational sum frequency generation
α	bulk phase α
β	bulk phase β

Symbols

Π	surface pressure
μ_i	chemical potential
A	area, molecular area
a	activity
B	magnetic field
C	surface concentration
c	speed of light
E	electric field
E₀	amplitude of the electric field

\mathbf{E}_i	electric field of the incident wave
\mathbf{E}_r	electric field of the reflected wave
\mathbf{E}_t	electric field of the transmitted wave
F	force
G	Gibbs free energy
g	gravitational constant
h	height of the plate
\mathbf{k}	wave propagation vector
k_b	Boltzmann constant
\mathbf{k}_i	wave vector of the incident wave
\mathbf{k}_r	wave vector of the reflected wave
\mathbf{k}_t	wave vector of the transmitted wave
L	length
m	mass, Gibbs adsorption coefficient
M	medium
M_w	molecular weight
n	refractive index, moles
P	pressure
R	universal gas constant, radius
\mathbf{r}	position vector
R_p	s -polarized reflectance
r_p	p -polarized Fresnel reflection coefficient
R_s	p -polarized reflectance
r_s	s -polarized Fresnel reflection coefficient
S	entropy
t	time
T	temperature, plate thickness, period
t_p	p -polarized Fresnel transmission coefficient
t_s	s -polarized Fresnel transmission coefficient
U	internal energy
V	volume

W	width
α	bulk phase α
β	bulk phase β
Γ	surface excess
γ_s	surface tension of surfactant monolayer
γ_w	surface tension of water
ε_r	phase constant of the reflected wave
ε_t	phase constant of the transmitted wave
θ	contact angle
κ	hygroscopicity parameter
λ	wavelength
ρ_l	density of liquid
ρ_p	density of plate
σ	interfacial region
ω	angular frequency

Introduction

1.1 Overview

Aerosols are the largest unknown factor in understanding climate change and the Earth's energy budget. They are involved in numerous processes such as cloud formation, ice nucleation, and heterogeneous surface reactions. Understanding aerosol properties such as size and composition and surface behavior is important in establishing climate models that accurately predict their effect on cooling in Earth's atmosphere. A large contributor of aerosols comes in the form of marine aerosols, as ~70% of the Earth's surface is ocean. Marine aerosols are created by wave shearing, tearing and bubble bursting at the surface.

The ocean surface itself is covered by a 1 mm-thick gelatinous film called the sea surface microlayer (SSML). The SSML is found to be enriched with organics, proteins, bacteria, algae and various other compounds. These compounds can reduce the surface tension of the ocean surface and affect the formation of marine aerosols. In addition, the SSML components can be incorporated into marine aerosols where they undergo further interactions at the surface of the aerosols.

Aerosols studies at the Center for Aerosol Impacts on Climate and the Environment (CAICE) based at University of California San Diego follow a multi-disciplinary approach to tackle the chemical complexity of aerosols in the laboratory to predict their impact on climate. To study the chemistry of aerosol surfaces, model

systems must be used, using molecules representative of the typical compounds found in marine aerosols. As a part of the efforts to understand aerosol complexity at CAICE, two molecules were chosen for our marine aerosol model: dipalmitoyl-phosphatidic acid (DPPA) and bacterial lipopolysaccharides (LPS).

DPPA is a type of diacylglyceride phospholipid, found as a breakdown product or precursor of larger cellular phospholipids. DPPA is involved in key cellular functions such as cell signaling and protein binding, and is present in the SSML from biomarine sources. DPPA contains no moieties on its phosphate headgroup, and thus is a simple model phospholipid for marine aerosol studies. Along with other researchers at CAICE, DPPA is being studied both experimentally and by simulations to understand its chemical behavior in the presence of common ocean cations.

In addition to DPPA, LPS was chosen as a representative molecule for bacterial interactions in aerosols. LPS is a complex lipoglycan found primarily in the cell walls of Gram-negative bacteria. LPS is crucial for maintaining the structural integrity of the cell walls and protecting the bacteria, as well as triggering inflammatory responses in animals. As bacteria interact with other organisms and die, LPS is released into the SSML and surfaces of marine aerosols.

As both molecules are chosen for their presence at the SSML, and ability to incorporate into aerosols, understanding their surface chemistry and interactions with each other and other surfactants is necessary to develop an understanding of aerosol impacts on climate. In this thesis, we study DPPA and LPS using Langmuir trough as a model for aerosol surfaces and image the surface using Brewster angle microscopy (BAM). Chapter 2 covers the theory of surface tensiometry and BAM, while Chapter 3

covers materials, and the experimental methods. Chapter 4 discusses the surface pressure-molecular area (Π -A) isotherm results and the corresponding BAM images. Chapter 5 summarizes work presently done, and what future work is needed.

1.2 Motivations

1.2.1 Aerosols on Climate

Climate change in the 21st century has been an important area of study. Due to anthropogenic influences, the rate of climate change in the last 200 years has increased dramatically. According to the latest Intergovernmental Panel on Climate Change (IPCC) report in 2013, most of the global warming since 1950 has been due to anthropogenic emissions.¹ Of the various factors that affect radiative forcing, aerosol effects are to date the largest source of uncertainty in total anthropogenic forcing (Figure 1.1). It is known that aerosols have a general cooling effect on our climate, but to an unknown degree.

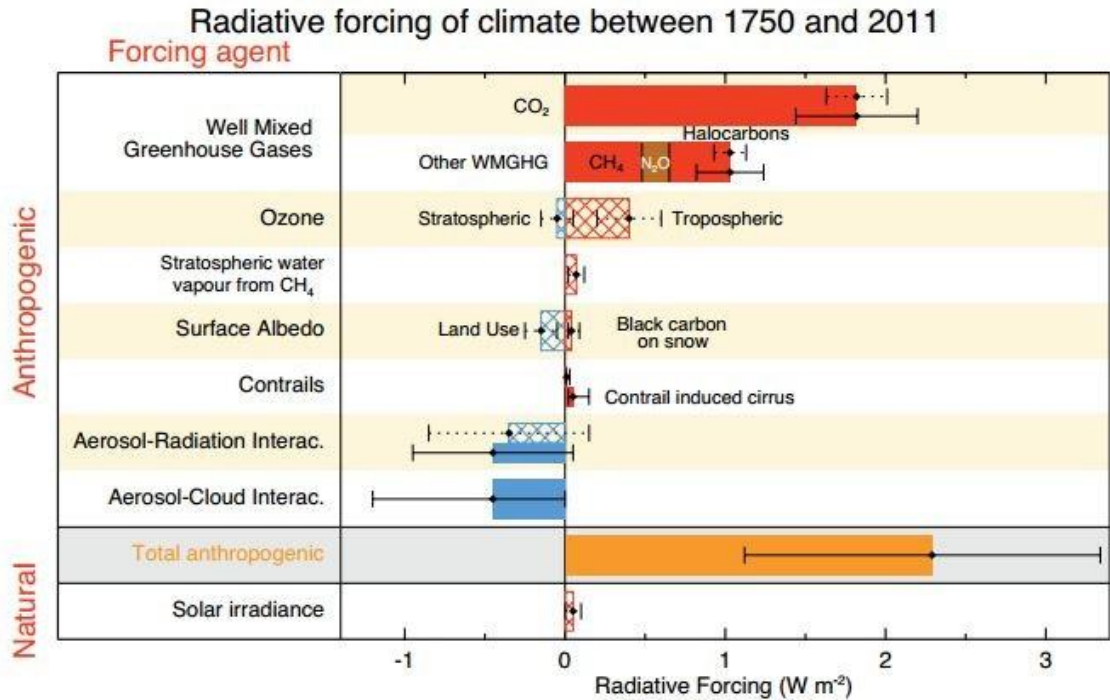


Figure 1.1 Bar chart for radiative forcing (hatched) and effective radiative forcing (solid). Uncertainties (5 to 95%) confidence range given in solid and dotted lines.¹

Aerosols affect climate in a myriad number of ways, directly and indirectly. Aerosols absorb and scatter solar radiation as well as thermal radiation. They act as cloud condensation and ice nuclei, and thus have an effect on the hydrological cycle.² Clouds themselves cover about 60% of the Earth and cool its atmosphere.³ The ability of aerosols to act as cloud condensation nuclei and form clouds is affected by their size, count, and composition.⁴ An increase in aerosols particle count can increase the initial cloud droplet number concentration (CDNC) and increase cooling by increasing the cloud optical depth by 1/3 the power of the change in CDNC.⁵⁻⁶ An increase in optical depth increases cloud albedo and reflectivity (Figure 1.2).⁷ In addition an increase in aerosol count can increase the number of cloud droplets affecting precipitation, cloud size, life-time and water content.

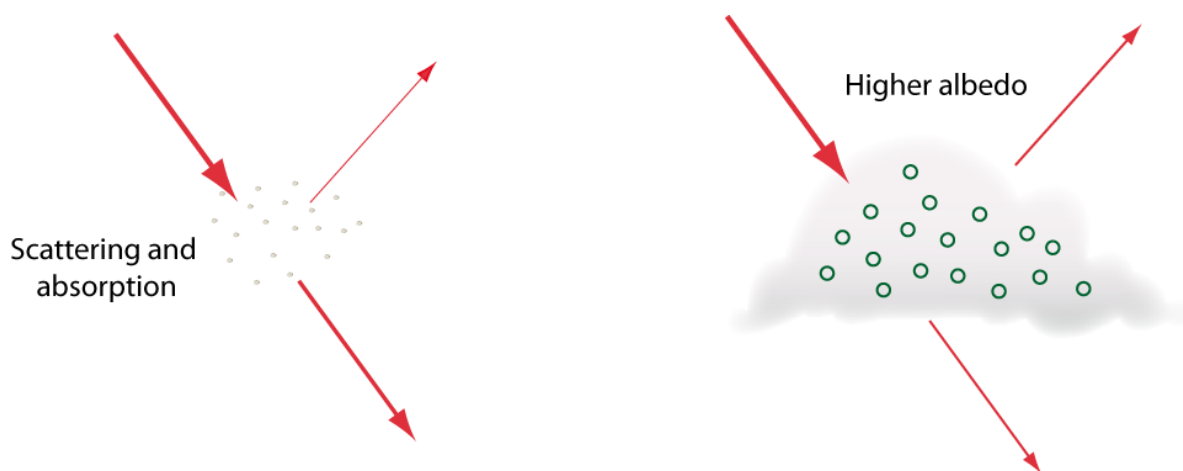


Figure 1.2 Schematic representation of direct and indirect cloud albedo effect.⁸

The radiative effect of aerosols is dependent on their type. Organic compounds are a significant component of atmospheric aerosols, and studies have been found aerosols to contain up to 50% organic compounds by mass.⁹⁻¹⁰ Organic compounds form thin films on the surface of aerosols and their presence affects aerosol volatility as well as rates of evaporation or growth.¹¹ This is modeled by their hygroscopicity parameter (κ), derived from Kohler theory which determines equilibrium conditions of aerosol droplet sizes, and the minimum size required to act as ice and cloud nuclei.¹² Laboratory experiments of insoluble and soluble monolayers on water surfaces have indeed found differences in evaporation rate.¹³⁻¹⁵ In addition, the organic films can affect a change in the absorbance and scattering of radiation by the aerosol, as well as participate in atmospheric relevant reactions.¹⁶⁻¹⁷ A large source of organics in these aerosols comes from marine aerosols, generated in the SSML.¹⁸⁻²⁰

1.2.2 Marine Aerosols and the SSML

The ocean surface covers 70% of Earth's land mass and is covered by a several mm-thick film called the sea surface micro-layer (Figure 1.3). The SSML is the boundary layer of the ocean and plays an important role in the heat and gas transfer at the ocean surface. It is involved in many complex physical, biological, chemical and photochemical interactions, and has been termed a bioreactor.²¹ Historically, the SSML has been thought to be comprised of a lipid layer on top, followed by a protein-saccharide layer. However, more recent evidence indicates the SSML is more akin to a gelatinous biofilm with a varied composition.²²⁻²⁴

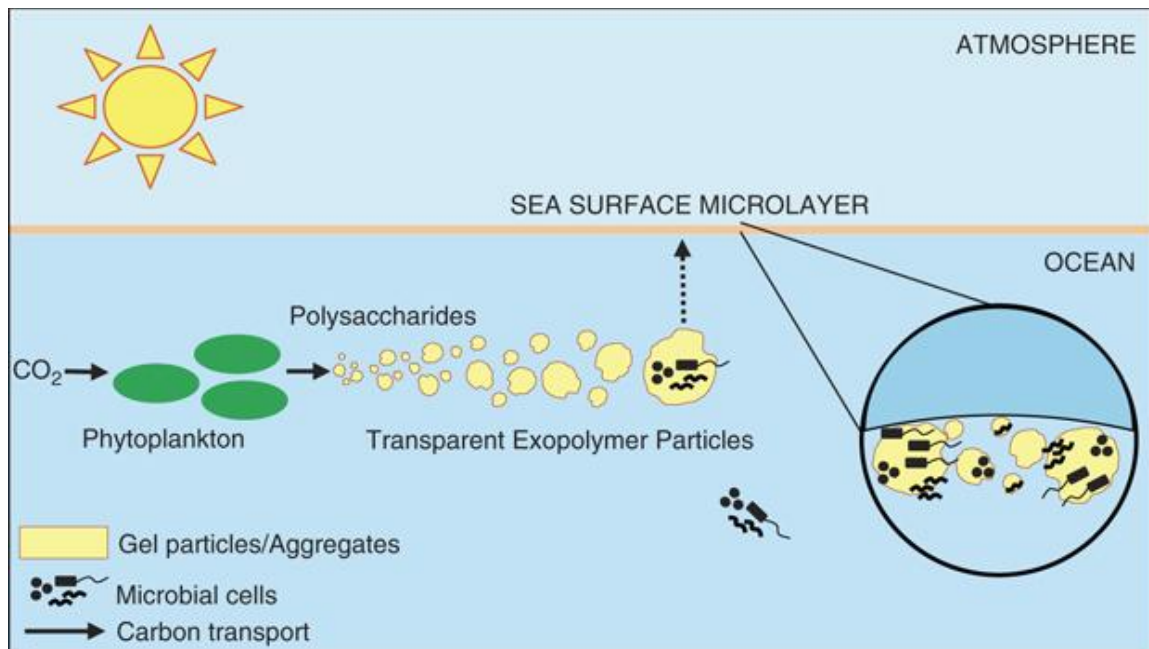


Figure 1.3 Representation of the SSML.²⁴

The exact composition and concentrations of these organics vary depending on the location and time of the year but primarily originate from biogenic sources such

marine organisms at the surface, as well as cellular debris from dying and decaying organisms rising to the surface.²⁵ The presence of algae, phytoplankton, bacteria, lipids, protein, amino acids, carbohydrates, polysaccharides and more have been found to be enriched in this biofilm.^{22, 24} These materials are incorporated into the surfaces of generated marine aerosols and imbue a seasonal characteristic to the physiochemical characteristics of marine aerosols.²⁶

Marine aerosols contribute a great deal to the global aerosol load. They are created by the action of wave breaking and drop tearing from the shearing action of wave motion, as well from bubble bursting from air entrained at the surface and from decomposition of organics.²⁷ These aerosols often consist of sea salt cores, and can pick up organic particles found at the ocean surface, particularly during bubble bursting.^{19-20, 28} In addition, the properties of marine aerosols are affected by these SSML components. Surfactants such as lipids and polysaccharides are known to reduce surface tension of liquid surfaces, which in turn can impede wave formation, affecting the number and size of marine aerosols produced.

1.2.3 Ion Relevance in Marine Aerosols

As marine aerosols often consist of a sea salt core with an organic coating, they display a wide range of sizes, compositions, morphologies and distribution of elements. The most common ocean cations are Na^+ , K^+ , Ca^{2+} , and Mg^{2+} , and their interaction with the organics incorporated from SSML materials affects the properties of these aerosols.²⁹ Aerosol compositions have been found to be size-dependent, and different combinations of cations and anions as well as the type of organic species have been found to affect

aerosol morphologies and crystallization behavior.³⁰ These differences between aerosols have implications for relevant atmospheric processes such as cloud and ice nucleation. In addition, studies have also found an effect of ions on the morphology and alkyl chain orientation, as well as the hydration state of headgroups of phospholipid monolayers at air-water surfaces.³¹⁻³³ Thus, the studies of ions with surfactants are models for the interactions of organic surfactant with the ions found in the interior bulk liquid of marine aerosols, and critical for understanding the chemical behavior of these aerosols.

1.2.4 DPPA and LPS Relevance

Phospholipids have been known to be enriched at the SSML, particularly as they comprise the cell membranes of biological organisms. Studies have found fatty acid lipids in both marine aerosols and ocean water. It is universally agreed that these fatty acids are of biological origin, in particular from marine sources, from the breakdown of phospholipids.³⁴⁻³⁶ Various sampling studies on the distribution of these fatty acids have found saturated C16 fatty acid, palmitic acid (PA), to be the most abundant, followed by saturated C14, C18 and an unsaturated C16:1 fatty acid with one double bond.³⁷⁻³⁹ PA is the breakdown product of common phospholipids, and is a component of DPPA. DPPA itself is an intermediate product of the breakdown of phospholipids by phospholipases, especially phospholipase D (PLD), which makes it an atmospherically relevant molecule of study.

Along with lipids, bacteria have been detected both on the surfaces of ocean and aerosols. Studies have detected Gram-negative bacteria such as *Streptomyces*, *Collimonas*, *Vibrio*, and *Pseudoalteromonas*, which contain cell walls with a large

percentage of LPS.⁴⁰⁻⁴¹ Thus LPS is likely to be found both in marine aerosols and ocean surfaces, particularly in situations of bacterial die-offs. In addition, studies have found LPS to bind and interact with surfactant proteins and phospholipids.⁴²⁻⁴³ Bacteria are also a major source of phospholipases, and contribute to the formation of DPPA and its fatty acid derivatives.⁴⁴

1.2.5 Mixing and Complexity

Aerosols are complex mixtures, and laboratory studies are challenged by ways to effectively model and study marine aerosols in the controlled lab environment. Global atmospheric models poorly characterize organic aerosols and the magnitude of their effects.⁴⁵ While field researchers are able to collect and sample ocean water and marine aerosols through ship and airplane measurements, a fundamental chemical understanding of the aerosol surfaces comes from simulated laboratory experiments of simple model systems. However, models based off parameters obtained in laboratory experiments still cannot explain the effects of organic aerosols, such as their aging and evolution, and their impact on climate.⁴⁶⁻⁴⁷ These separate top-down and bottom-up approaches suffer from a lack of information sharing such as the chemical composition of relevant aerosols, and the chemical behavior of the aerosol constituents. Thus the goal of CAICE is to bridge field researchers who study the composition and behavior of these complex aerosol systems with lab experimentalists who study the chemistry of these aerosol systems using simple models to bring a unified understanding of the chemical nature and behavior of aerosols and their impact of climate change. As part of the mission of CAICE, fundamental chemical studies of DPPA in this thesis are done in collaboration with

theoretical research groups who support and are supported in their simulation studies of DPPA such as the group of Dr. Francesco Paesani at the University of California: San Diego. As part of this joint approach, DPPA and LPS were selected as ideal representative model molecules of organic surfactants likely to be found in marine aerosols. Understanding the chemistry of DPPA in particular, as an intermediate phospholipid, is a step in understanding the behavior of more complex phospholipids. In addition, as the marine aerosol system is a complex mixture, the simple model systems studied will need to increase in complexity to better model the real systems of interest.

1.3 Surfactants

Surfactants refer to molecules that are active at a surface. They are characterized by their ability to adsorb to interfaces, such as aqueous surfaces. This is due to their amphipathic nature, having polar and nonpolar groups. The polar group may carry a positive or negative charge, as is the case for cationic or anionic surfactants, both for zwitterionic surfactants, or no charge at all such as ethylene oxide chains or sugar or saccharides.⁴⁸ The driving force of a surfactant is lowering its free energy, which is achieved by residing at the interface. Surfactants are abundant in living organisms, such as lipids and lipopolysaccharides, and thus are ecologically important.

1.3.1 Phospholipids

The cellular membrane is composed of a lipid bilayer, with three primary classes of compounds: phospholipids, glycolipids, and sterols. In addition to lipids, carbohydrates

and proteins also comprise a major portion of the cell membrane. This is referred to as the fluid mosaic model of the cell plasma membrane (Figure 1.4).

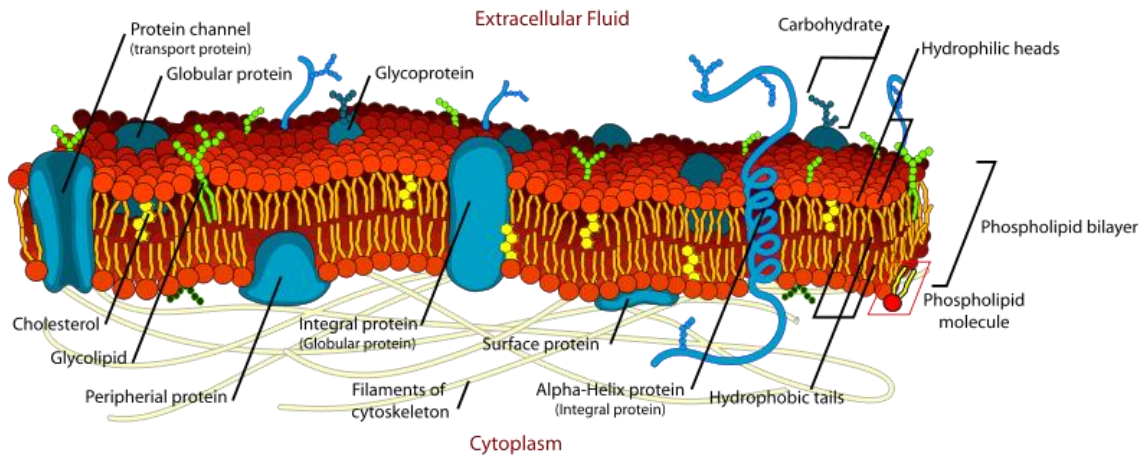


Figure 1.4 Diagram of cell membrane. (Adapted from Wikimedia commons file “Cell_membrane_detailed_diagram_4.svg”)

Among the membrane lipids, phospholipids are the most abundant. The most common phospholipid structures are diacylglycerides. The structure of a diacylglyceride consists of two fatty acid chains bonded to a glycerol backbone which is connected to a phosphate group with possible additional moieties. For mammalian cells, the outer leaflet of the lipid bilayers contains primarily phosphatidylcholine (PC), while the inner leaflet contains phosphatidylethanolamine (PE), phosphatidylserine (PS), and phosphatidylinositol (PI) and its phosphorylated derivatives (PIP₂, PIP).

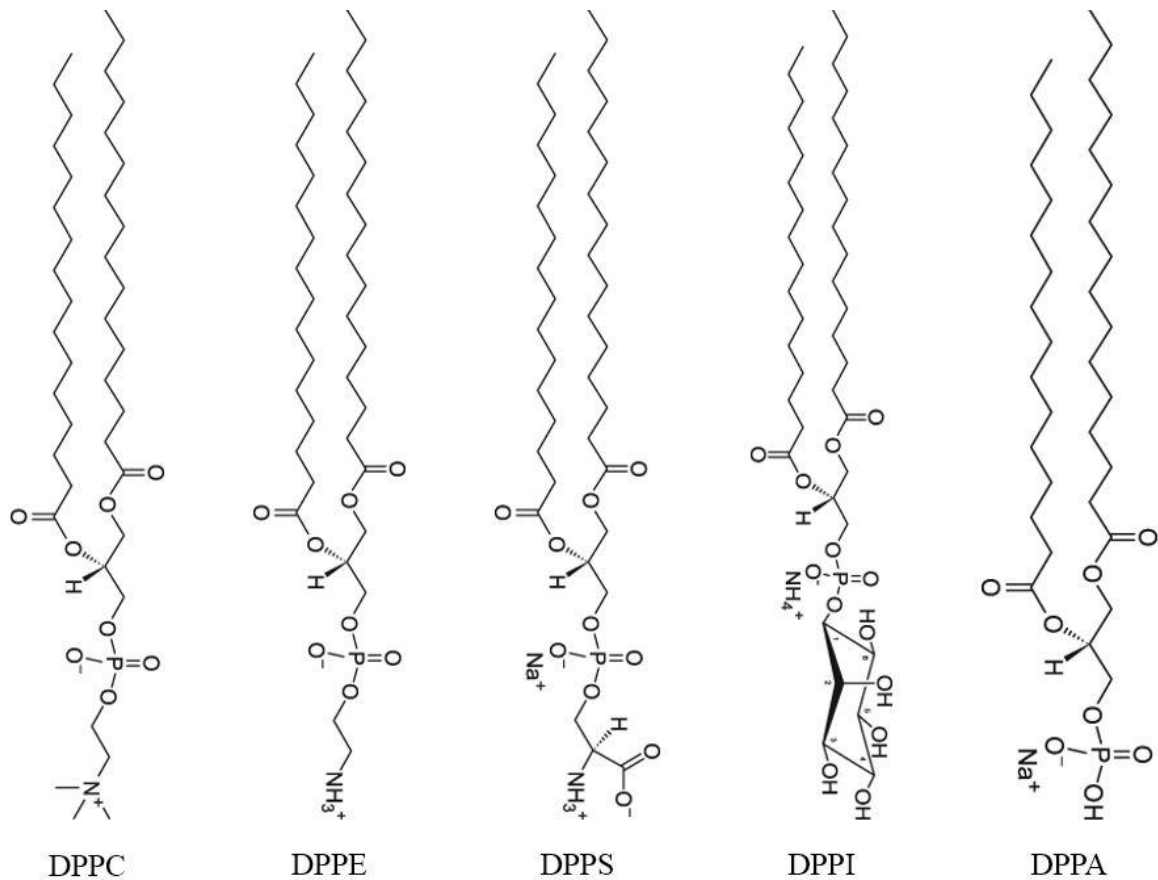


Figure 1.5 Structures of common membrane lipids.

One of the key functions of cell membranes is regulating the flow of ions and maintaining an ion gradient between the interior and exterior of the cell. For example the cytoplasm of the cell contains higher concentrations of K^+ , while the extracellular space contains higher concentrations of Na^+ . Other crucial ions include Ca^{2+} , Mg^{2+} , Cl^- , CO_3^{2-} , and PO_4^{3-} . This concentration gradient of ions is controlled by various cell features such as ion channels for passive transport and ion pumps for active transport. Changes in these ion gradients allow cells to change their electric potential across the membrane allowing them to do work such as ATP production, cell signaling and various other functions. Thus

an understanding of the interactions of the cell membrane phospholipids with these ions is extremely biologically important.

1.3.2 DPPA

DPPA is a key phospholipid for maintenance of cell membranes. As shown in Figure 1.5, it consists of two palmitic acid chains bonded to a glycerol backbone, bonded to a phosphate headgroup; the very definition of a diacylglyceride. Although it exists in only small amounts due to its high turnover rate (~1%), it is an absolutely critical bioactive lipid.⁴⁹ As a simple phospholipid, it is a key metabolite in the synthesis of larger cell membrane phospholipids such as PC, PE, PS and PI. Likewise, it is also involved in the breakdown of phospholipids as well as other functions such as membrane dynamics, i.e. fission and fusion, and implicated in cell signaling via its interactions with other phospholipids or the binding of proteins.⁵⁰⁻⁵¹

Studies have shown DPPA to be sensitive to hydrogen bonding, electrostatic interactions, and pH conditions, which all affect its ionization state.⁵² DPPA can vary its charge from neutral to 2⁻ based on the protonation of its phosphate headgroup. This has been termed the electrostatic/hydrogen-bond switch, in which hydrogen bonding induces deprotonation of the phosphate headgroup, leading to a change in protein binding affinity.⁵³⁻⁵⁴ Thus an understanding of the effect of specific ions and ionization states on DPPA monolayers can shed light on its key biological functions.

The presence of DPPA is highly regulated by phospholipases. Phospholipases are enzymes that are widely distributed in eukaryotes and prokaryotes and are sorted into classes based on where cleavage occurs along the phospholipid. Phospholipases A and B

(PLA, PLB) cleave the acyl chains, phospholipase C (PLC) cleave right before the phosphate, and PLD cleaves right after the phosphate. The hydrolysis of any phospholipid by PLD generates DPPA.⁵⁵⁻⁵⁸

1.3.3 LPS

Bacterial LPS are a class of compounds consisting of lipids covalently bonded to polysaccharides. They comprise the majority of composition of the outer cell walls of Gram-negative bacteria.⁵⁹ Gram-negative bacteria refer to a class of bacteria that do not stain violet in Gram-staining tests, which tests for the presence of peptidoglycan. While Gram-positive bacteria have a thick layer of peptidoglycan, Gram-negative do not but instead contain LPS in their outer membrane. Most common bacteria are Gram-negative such as *Escherichia Coli*, *Salmonella*, *Shigella*, and *Pseudomonas*. LPS serves to protect the bacteria from damage such as antibiotics, virus invasion, or lysing by detergents.⁶⁰ When released into the circulatory system, LPS acts as an endotoxin. In small amounts, it has been considered beneficial in stimulating the immune system in uses such as shrinking tumors.⁶¹ However, as an endotoxin, effects include fever, elevated heart rate, and larger amounts can lead to septic shock and death organ failure and systemic inflammatory response.⁶²⁻⁶³

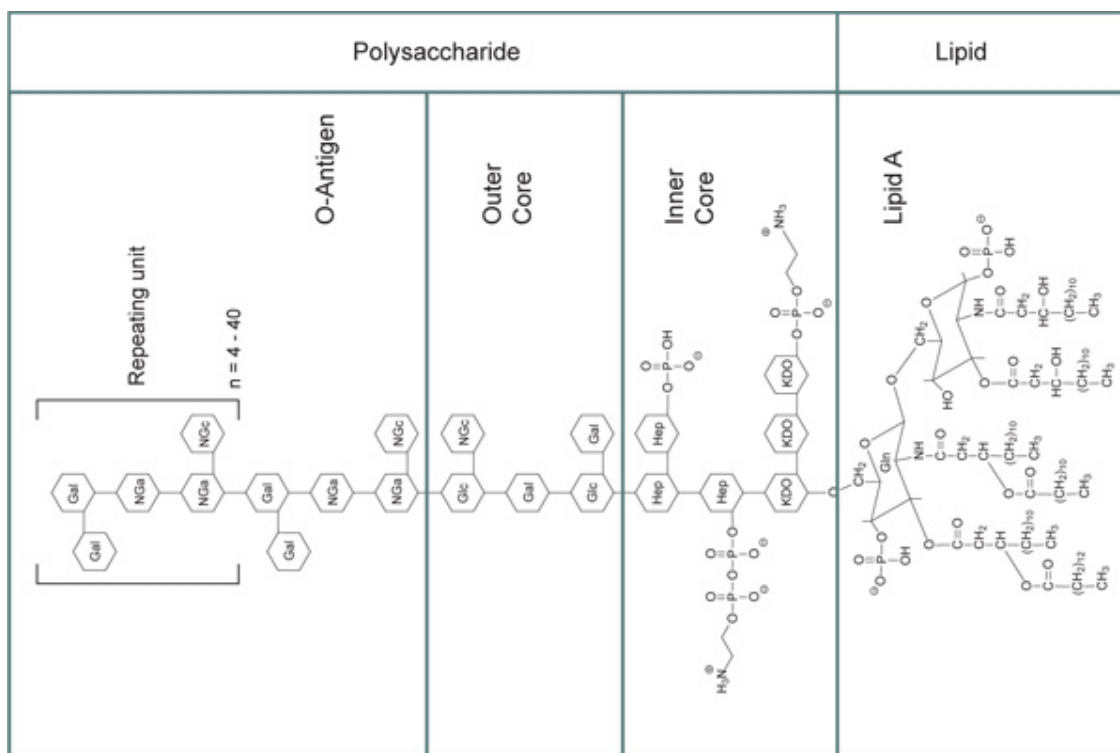


Figure 1.6 General structure of LPS

<http://www.sigmaldrich.com/technical->

<documents/articles/biology/glycobiology/lipopolysaccharides.html>

LPS has been shown in studies to be surface-active.⁶⁴⁻⁶⁵ However, it is a large molecule as seen in Fig. 1.6 and resists structural characterization. Due to its amphipathic nature, it has a tendency to aggregate and form structures like micelles, making it difficult to determine a molecular weight.⁶⁶⁻⁶⁷ The presence of cations can cause intermolecular cross-linking in addition to the various hydrophobic interactions.⁶⁸ LPS structure can vary between bacteria, and even between different populations of the same strain. As shown in Figure 1.6, LPS consists of a Lipid-A core and a polysaccharide core followed by a variable length O-antigen polysaccharide chain.⁶⁹ LPS is categorized as rough or smooth depending on the length of the O-antigen, with smooth having the full length chain, and

rough having shortened or missing O-antigen chains.⁷⁰ Thus precise identification of the molecular weight of LPS requires mass spectrometry, and even that is complicated by the heterogeneity of LPS, as bacteria can contain both the smooth and rough forms.⁶⁴

1.4 Objectives

In this study, Langmuir monolayers were used as the laboratory model of DPPA for cell membranes and aerosol surfaces. Preliminary studies of LPS as Gibbs monolayers were also done. The primary focus of this study is the interaction of DPPA with ions at various ionization states. Chapters 2 and 3 discuss the methods and techniques used in these studies, surface tensiometry and BAM. Chapter 4 discusses the results on DPPA monolayer organization, mechanism formation, and morphology.

Chapter 2: Theory and Instrumentation

2.1 Surface Tensiometry

2.1.1 Gibbs Adsorption Equation

To understand the thermodynamics of monolayers, one can think of the system as two bulk phases separated by an interface. One approach, the Gibbs convention, treats the interface as infinitesimally thin line with no volume called the Gibbs dividing surface (GDS). However, in a real system, the interface is not a plane, but an extended inhomogeneous region with a volume. Guggenheim explicitly treated the extended interface with a volume, but for mathematical simplicity and practicality, the Gibbs approach is used as both lead to similar results.

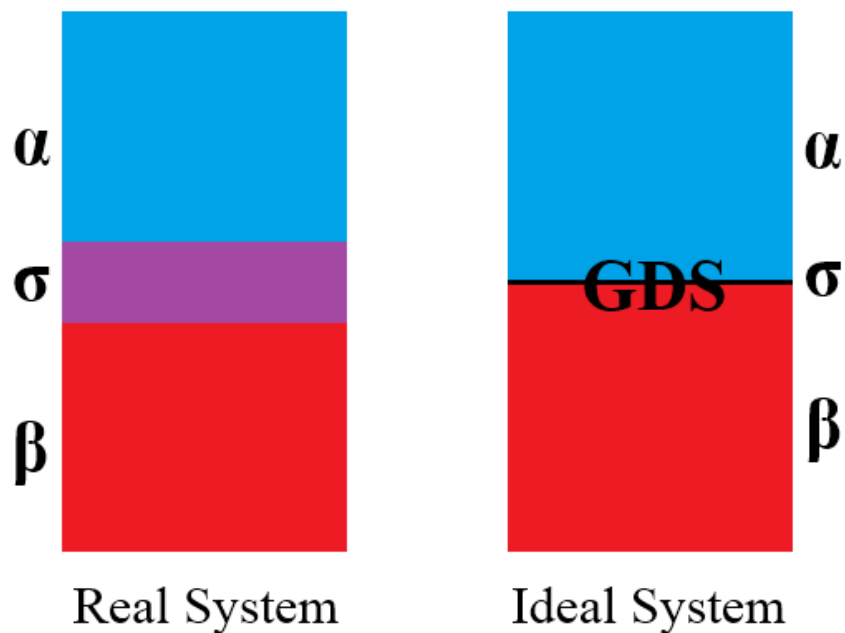


Figure 2.1 The interface between two bulk phases of real and ideal systems.

The system is divided into bulk phases α and β and the interface σ where the GDS lies. The GDS is arbitrarily placed, and the extensive properties of the system can be treated as the sum of the three components. The total internal energy U , total Gibbs free energy G , and total number of components of i -th substance n_i , for example can be given as

$$U = U^\alpha + U^\beta + U^\sigma \quad (2.1)$$

$$G = G^\alpha + G^\beta + G^\sigma \quad (2.2)$$

$$n_i = n_i^\alpha + n_i^\beta + n_i^\sigma \quad (2.3)$$

In the ideal system, the amount of components n_i in each bulk phase depends on the placement of the GDS, and interface is treated as having none, since it has no volume. However, in a real system, the amount of components in the bulk phases can be different from that of the ideal reference system, and the difference is located at the interface. Thus, this difference is defined as the surface excess, which is the concentration of components at the surface. The concentration of molecules at the interface can be given as the number of molecules at the surface, n_i , divided by the interfacial area A .

$$\Gamma = \frac{n_i}{A} \quad (2.4)$$

The change in internal energy of the system according to the first and second principle of thermodynamics, can be expressed by the thermodynamic definition

$$dU = TdS - PdV + \sum u_i dn_i + dW \quad (2.5)$$

where T is the temperature, S is the entropy, P is the pressure, V is the volume, μ_i is the chemical potential, and W the work done on the system without expansion work PdV .

According to Eq. (2.1), Eq. (2.5) can be broken down to its components

$$dU^\alpha = TdS^\alpha - P^\alpha dV^\alpha + \sum \mu_i dn_i^\alpha \quad (2.6)$$

$$dU^\beta = TdS^\beta - P^\beta dV^\beta + \sum \mu_i dn_i^\beta \quad (2.7)$$

$$dU^\sigma = TdS^\sigma + \sum \mu_i dn_i^\sigma + \gamma dA \quad (2.8)$$

where PdV is the volume work done by the two bulk phases. As the interface has no volume, it cannot perform volume work, but contains the surface work term γdA , as the work done to change the surface area is proportional to the change in area and surface tension.

We are interested in the interfacial region, and dU^σ can be integrated due to Euler's theorem. Physically, this means since U^σ is a linear function of S^σ , n_i^σ , and A , if all other constants are kept constant, the internal energy of the surface can be increased by increasing S^σ , n_i^σ , and A in proportion. Thus we have

$$U^\sigma = TS^\sigma + \sum \mu_i n_i^\sigma + \gamma dA \quad (2.9)$$

We can differentiate Eq. (2.9) to get

$$dU^\sigma = TdS^\sigma + S^\sigma dT + \sum \mu_i dn_i^\sigma + \sum n_i^\sigma d\mu_i + \gamma dA + Ad\gamma \quad (2.10)$$

If we combine Eqs. (2.8) and (2.10), we get

$$S^\sigma dT + \sum n_i^\sigma d\mu_i + Ad\gamma = 0 \quad (2.11)$$

At constant temperature, Eq. (2.11) simplifies to

$$\sum n_i^\sigma d\mu_i + Ad\gamma = 0 \quad (2.12)$$

Further rearrangement leads to

$$d\gamma = - \sum \frac{n_i^\sigma}{A} d\mu_i \quad (2.13)$$

According to Eq. (2.4), this can be further simplified to

$$d\gamma = - \sum \Gamma d\mu_i \quad (2.14)$$

In a two-component system,

$$d\gamma = - \sum \Gamma_1 d\mu_1 - \sum \Gamma_2 d\mu_2 \quad (2.15)$$

The value of Γ is defined relative to the arbitrarily chosen GDS. If we set fix the GDS so that $\Gamma_1 = 0$, Eq. (2.15) simplifies to

$$\Gamma_2 = - \frac{d\gamma}{d\mu_2} \quad (2.16)$$

The chemical potential μ is defined by the equation

$$\mu_2 = \mu_2^\circ + RT \ln(a_2) \quad (2.17)$$

where μ_2° is the chemical potential of the standard state, R the universal gas constant, and a the activity. Differentiation of the chemical potential gives the equation

$$d\mu_2 = RT \frac{da_2}{a_2} \quad (2.18)$$

Substitution of Eq. (2.18) into Eq. (2.16) gives

$$\Gamma_2 = - \frac{a_2}{RT} \frac{d\gamma}{da_2} \quad (2.19)$$

Eqs. (2.18) and (2.19) are known as the Gibbs adsorption isotherm.

2.1.2 Surface Free Energy and Surface Tension

As mentioned earlier, the interface is inhomogeneous and has its own thermodynamic properties separate from the bulk. From the internal energy of the

surface, we can derive the Gibbs free energy of the surface with the simple thermodynamic relationship

$$G = U - TS + PV \quad (2.20)$$

Thus Eq (2.8) can be written in terms of G as

$$dG^\sigma = -S^\sigma dT + V^\sigma dP + \sum \mu_i dn_i^\sigma + \gamma dA \quad (2.21)$$

This can be expressed as the sum of partial differentials where

$$dG = \left(\frac{dG}{dT}\right)_{P,n_i,A} dT + \left(\frac{dG}{dP}\right)_{T,n_i,A} dP + \left(\frac{dG}{dn_i}\right)_{P,T,A} dn_i + \left(\frac{dG}{dA}\right)_{P,T,n_i} dA \quad (2.22)$$

From Eqs. (2.21) and (2.22), it can be seen that

$$\gamma = \left(\frac{dG}{dA}\right)_{P,T,n_i} \quad (2.23)$$

Thus, surface tension is the work it takes to change the area of the surface under reversible and isothermal conditions.

A physical explanation of surface tension is that of the excess free energy of the surface. In the bulk of a liquid phase, the molecules are isotropic and each molecule feels an equal force from the neighboring molecules from all directions. Thus the net force felt by the molecule is zero. At the interface, this symmetry is broken, and the molecule is not surrounded on all sides. Thus, the net force is non-zero and the molecule is pulled towards other molecules adjacent on the surface. In response, the system pulls the molecules into the bulk to reduce this excess energy, or contracts into circular domains to reduce the surface area.

2.1.3 Method of Measuring Surface Tension

The method of measuring surface tension in this study is the Langmuir-Wilhelmy balance (LWB). Although neither the best nor the only method of measuring surface tension, the LWB does have many advantages as well as disadvantages compared to other methods, as well as being the most common.

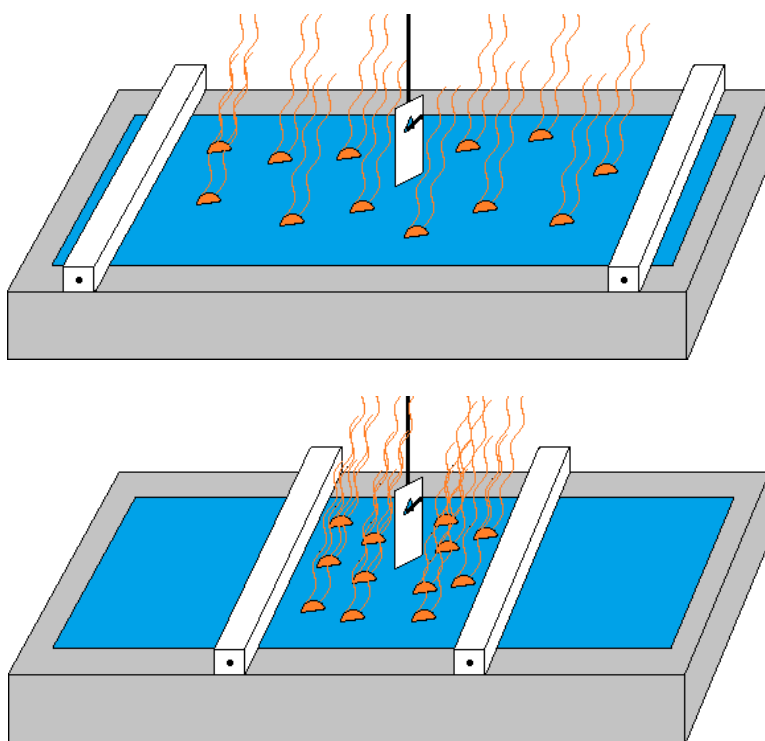


Figure 2.2 Schematic diagram of Langmuir trough with Wilhelmy plate open and closed.

The LWB method typically is comprised of a Langmuir trough, movable barriers and a Wilhelmy plate tensiometer. The Langmuir trough is filled with a liquid called the subphase, typically water. The surfactant molecule of interest is dissolved in an organic solvent, such as chloroform or methanol, and deposited on the surface dropwise. The

organic solvent spreads across the surface and evaporates, leaving behind a monolayer of the sample on the surface. This dropwise technique is called “spreading” and involves a certain degree of manual skill.

Movable barriers compress and expand the spread monolayer, changing the density of the molecules on the surface. Common barriers can include hydrophilic blocks, or thin ribbons of various materials. This change in density results in changes in the surface pressure, which is detected by the tensiometer. Surface pressure is a value related to surface tension and given by:

$$\pi = \gamma_w - \gamma_s \quad (2.24)$$

where γ_w is the surface tension of the subphase and γ_s is the surface tension of the subphase with a monolayer.

The tensiometer measures the surface pressure using the Wilhelmy plate method. Traditionally, the Wilhelmy plate is made of platinum due to its sensitivity, and ease of cleaning of organics via flaming. Typically, the Wilhelmy plate is a piece of absorbent paper, such as filter paper which is commonly used. The Wilhelmy plate is wetted to ensure a contact angle of 90° , and suspended so the plate is partially immersed in the subphase. The tensiometer measures the net forces acting on the plate, which include gravity and surface tension pulling downwards, and buoyancy pushing upwards. The net force (F) is dependent on the width (W), length (L), and thickness (T) of the plate, and is given by the equation

$$F_{net} = \rho_p g L W T + 2\gamma(T + W) \cos \theta - \rho_l g T W h \quad (2.25)$$

where ρ_p and ρ_l are the densities of the plate and liquid respectively, g the gravitational constant, θ the contact angle, and h the immersed height.

For typical use, the plate is assumed to be completely wetted to ensure a contact angle of 90° , so $\cos(90^\circ) = 1$. The plate can be held stationary at a constant h , and thus change in the net force corresponds to change in the second term, assuming the liquid and plate parameters remain constant. Eq. (2.25) can thus be rearranged to give surface tension as a function of the net force, width and thickness.

$$\Pi = -\Delta\gamma = -\frac{\Delta F}{2(T + W)} \quad (2.26)$$

Commonly, the tensiometer acts like a balance, and the measured mass (m) can be multiplied by the gravitational constant to get the force.

$$F = mg \quad (2.27)$$

We assume the plate is thin enough such that T can be neglected and the simplified equation allowing for calculation of surface tension is

$$\Pi = -\Delta\gamma = -\frac{mg}{2W} \quad (2.28)$$

where m is the mass measured by the tensiometer. In short, the tensiometer acts as a very sensitive balance, and knowing the width of the balance paper, along with the gravitational constant and the recorded mass allows calculation of the surface pressure.

The LWB trough is the most common method of surface tension, due to its many advantages. Experimental conditions such as subphase composition, compression rate, and temperature can be easily modified. The LWB trough encompasses a large area allowing for simultaneous studies with other instruments such as imaging or spectroscopic techniques. Disadvantages to the LWB trough method, include a large area requiring a large volume of subphase material, and an inability to compress the monolayer rapidly. Leakage of the sample and subphase over the edges of the trough is common, although the use of hydrophobic materials such as Teflon have reduced but not

eliminated this problem. Surface tension measurements are highly sensitive to the presence of contaminants, so cleanliness of the trough, subphase, and interface is crucial.

Other methods of measuring surface tension exist, with their own advantages and disadvantages compared with the Wilhelmy plate method. Such methods include the classic pendant drop (PD) and constrained sessile drop (CSD) which calculate the surface tension of low volume droplets from their size and shape using the Laplace-Young equation

$$\Delta P = \gamma \left(\frac{1}{R_1} + \frac{1}{R_2} \right) \quad (2.29)$$

where ΔP is the pressure differential across the droplet and R_1 and R_2 are the inner and outer radii of the droplet respectively. Other non-droplet techniques include the traditional Du-Noüy Ring method, which behaves similarly to the Wilhelmy plate method, using a ring as the probe. These methods will not be discussed in detail within the scope of this discussion.

2.1.4 Langmuir and Gibbs Monolayers.

Langmuir monolayers are the classic example of monolayers formed by amphipathic molecules such as DPPA. They are insoluble and thus are not in equilibrium with the bulk. The Gibbs adsorption equation is not applicable to Langmuir monolayers, but since they are confined to the interface, compression leads to changes in surface tension. However, there is another class of monolayer, of soluble surfactants, called Gibbs monolayers. Gibbs monolayers adsorb to the interface from one of the bulk phases, and thus are in equilibrium. Thus the Gibbs adsorption isotherm can relate the surface tension to the surface concentration. However, there is little difference in the treatment of

Langmuir and Gibbs monolayers. For dilute solutions, the surface tension of a Gibbs monolayer is given by

$$\gamma = \gamma_0 - mC \quad (2.30)$$

where m is the coefficient of Gibbs adsorption, and C the surface concentration.

2.1.5 Isotherms and Phases

Langmuir monolayer studies provide useful information other than just surface tension. Henri Devaux, shortly after 1900, observed that molecules in monolayers existed in quasi 2-D states analogous to that of 3-D liquids, solids or gases. A change in the temperature or surface pressure can transform the phase of a 2-D monolayer, such as from a gas to a liquid. Just as changing the pressure of a gas can change its phase, so can changing the surface pressure of monolayer. The surface pressure, while defined as the excess free energy of the surface, is a measure of the various forces between the molecules of a monolayer. As pressure is often plotted against volume at a constant temperature, so too is surface pressure plotted against the mean molecular area. The mean molecular area is the average free space each molecule in a monolayer has to occupy. It can be viewed as the 2-D analog of volume, just as surface pressure is the 2-D analog of pressure. A decrease in the mean molecular area when a monolayer is compressed results from a reduction in space occupied by a single molecule. As the molecules get closer, increased interactions change the surface pressure, just as they would in a 3-D phase.

A surface pressure-area isotherm (Π -A) isotherm gives such information about a monolayer such as its phase and degree of interaction between the molecules. The shape of the isotherm is dependent on the chemical nature of the monolayer, as it determines the

type and magnitude of forces at the surface. Such surface forces include attractive van der Waals forces (broken down into permanent dipole, induced dipole, and London dispersion forces), repulsive electrostatic double-layer forces, solvation forces, hydration forces, steric interactions, and hydrogen bonding. The possible 2-D phases observed in Π - A isotherms are discussed below.

Gaseous Phase

When the molecules in a Langmuir monolayers are spread very far apart, they exert little force on one another. This conceptually is similar to that of a gaseous state. In the gas phase, surface pressure is almost undetectable. The behavior of the gaseous phase (G) is treated as a two-dimensional kinetic analysis corresponding to traditional three-dimensional ideal gas theory. Thus, the molecules move with an average translational kinetic energy of $\frac{1}{2}k_bT$ for each degree of freedom, where k_b is the Boltzmann constant. For a 2-D surface such as the Langmuir monolayer, the total kinetic energy is k_bT , and is assumed to be the source of surface pressure. Thus,

$$\Pi A = k_b T \quad (2.31)$$

where A is the mean molecular area.

Liquid Phases

As the monolayer is condensed, the molecules can enter a first-order phase transition into the liquid state. In this liquid state, there is significant lateral interaction compared to the negligible interaction in the gas phase. There are two types of liquid phase, the liquid-expanded (LE) and liquid-condensed (LC) phase. In the LE phase

transition, the Π - A isotherms display a considerable curvature at liftoff from $\Pi = 0$ mN/m. The headgroups are still hydrated, and for long chain fatty acids, the area can be around 40-70 \AA^2 .

As the molecules are compressed even further, they can undergo another first-order phase transition into the LC phase. This is typically preceded by a straight horizontal line called the LE-LC coexistence region, where both the LE and LC phases are in equilibrium with each other. This occurs when the Gibbs free energy for both phases are equal to each other. During the LE-LC coexistence region, the density is an intermediate between that of the two phases.

The LC phase transition itself is usually marked by a sharp steep slope indicating reduced compressibility. During the LC phase, the headgroups are more dehydrated, and there is increased interaction between the tails. The LC phase can be further divided into two phases, marked by a kink in the sharp slopes, called the tilted-condensed (TC) and untilted-condensed (UC). The first TC phase of the LC region describes when the alkyl chains are closely packed but tilted with respect to the surface. As the monolayer is compressed further, the chains orient themselves completely perpendicular to the surface and are untilted.

Solid Phase

Further compression of the monolayer can result in a solid-like phase. In the solid phase (S), the headgroups are dehydrated, and the tails are so tightly packed the area corresponds to the molecular cross-section. Further compression is extremely difficult, and the molecules are strongly interacting with each other.

Collapse Phase

As the monolayer is compressed, at a certain point the film can no longer be compressed any further. The monolayer is disrupted, and can buckle, break or be forced into the bulk liquid. Two types of collapse phase exist, constant-area collapse and constant-pressure collapse. Constant area collapses are noted by a sharp decrease in surface pressure, while constant-pressure collapse is noted by a horizontal or slightly rising value in surface pressure. Whether the collapse is reversible depends on the collapse mechanism.

The collapse mechanism is dependent on the chemical nature of the film, the temperature and the compression speed. If the monolayer is forced into the bulk subphase, collapse is irreversible. This typically happens to fluid films. For more rigid films, the monolayer can form 3-D aggregates in the air side of the film. These aggregates are stable, so collapse is not reversible and reincorporation of the monolayer not possible. Imaging techniques such as BAM, as well as X-ray diffraction studies have found a wide variety of structures not limited to vesicles, bilayers, and trilayers.

One method of reversible collapse is known; folding. When the monolayer is compressed until it buckles, these buckles into the air can coexist with the flat portions of the monolayer until further compression forms 3-D aggregates. Folding is very sensitive to experimental conditions and may not happen or be reversible.

2.2 Brewster Angle Microscopy

Brewster Angle Microscopy is a surface imaging technique that takes advantage of the phenomena that occurs at the Brewster angle. The Brewster angle is the angle of incidence at which p -polarized light is perfectly transmitted through a transparent dielectric surface. This is dependent on the refractive index of the surface. When a light source and detector are positioned at the Brewster angle of the surface in question, reflection is at the absolute minimum, and nothing is seen. A change in the surface, such as the presence of a monolayer, changes the refractive index of the surface, and thus allows light to be reflected off the surface into the detector. BAM provides morphological information similar to that provided by fluorescence microscopy, however, the sample does not need to be auto-fluorescent nor is a fluorescent probe needed. Further explanation of the principles and theory of BAM imaging will be discussed in the following sections.

2.2.1 Plane Harmonic Waves

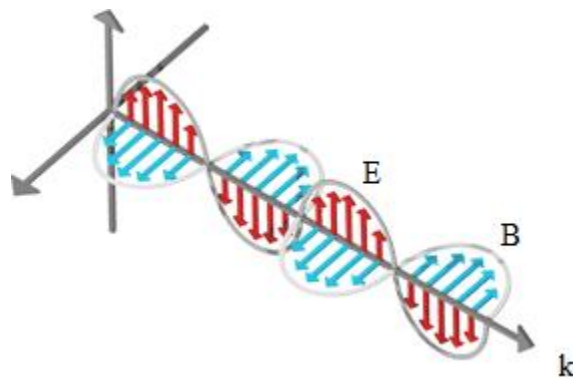


Figure 2.3 Diagram of electromagnetic wave.

Light is an electromagnetic (EM) wave propagating through a medium. According to Maxwell's laws, a temporally varying electric field is always associated in

phase with a spatially varying magnetic field, and vice versa. Thus, light is a transverse wave composed of electric field (\mathbf{E}) and magnetic field (\mathbf{B}) vectors, at a fixed intensity ratio, which oscillate perpendicularly to each other, and perpendicularly to the direction of propagation, denoted by the propagation vector (\mathbf{k}). If the electric field oscillates sinusoidally in time, and is constant over the direction of propagation, it can be viewed as a plane harmonic wave. Visually, it can be described as an infinite number of \mathbf{E} field planes perpendicular to \mathbf{k} and moving along it. A plane harmonic wave can be mathematically described as

$$\mathbf{E}(\mathbf{r}, t) = \mathbf{E}_0 e^{i(\mathbf{k}\mathbf{r} - \omega t)} \quad (2.32)$$

where E_0 is the amplitude of the electric field, \mathbf{k} is the wave propagation vector, \mathbf{r} is the position vector, and ω is the angular frequency which equals $2\pi/T$, where T is the period of the electric field.

2.2.2 Polarization States

Light as an EM wave has an oscillating electric field. When the electric field has a direction, the light is polarized. A polarized electric field can be broken down into two perpendicular components, often along the x - and y - axis (e.g., E_x and E_y) or parallel and perpendicular to the plane of incidence (e.g., E_p and E_s). In the latter case, the components are referred to as p - and s -polarized. The electric field can have further polarization states with different combinations of amplitude and relative phases of these two components. When the two perpendicular components such as E_p and E_s are equal in amplitude and in phase by 0° or 180° , or if one of components amplitude is zero such as light that is exclusively p -polarized, the light is linearly polarized. If the two components

are equal in amplitude but have phase difference of 90° , the light is circular polarized, as the \mathbf{E} field oscillating over time will trace a circle. If the two components have different amplitudes, or relative phases other than 0° , 90° or 180° , or both, the \mathbf{E} field will trace an ellipse and is thus elliptically polarized.

2.2.3 Reflection and Refraction

When a plane harmonic wave impinges at an incident angle of θ_i on an interface of two mediums, M_1 and M_2 , with different refractive indices n_1 and n_2 , part of the wave is reflected, part transmitted, and part reflected. For most cases, both media are dielectric, and the absorption is negligible. Thus, an incident wave impinging at the interface between these two media is broken down into reflected and refracted waves. As shown in Fig. 2.4, the incident wave impinges at an angle θ_i , is reflected at θ_r , and refracted in M_2 at θ_t .

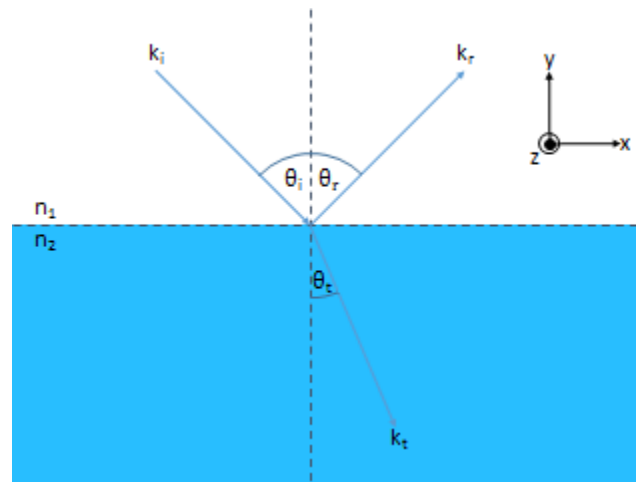


Figure 2.4 Reflection and refraction of a plane-harmonic wave at an interface.

Maxwell's laws lead to requirements for fields at interfaces, called boundary conditions. Specifically, the tangential components (the x and z axes in Figure 2.4) of the

electric fields must be equal across the interface, or in other words the total tangential component on one side of the interface must be equal to that on the other side. This can be mathematically represented as

$$\mathbf{E}_i(\mathbf{x}, t) + \mathbf{E}_r(\mathbf{x}, t) = \mathbf{E}_t(\mathbf{x}, t) \quad (2.33)$$

where \mathbf{E}_i , \mathbf{E}_r , \mathbf{E}_t are the incident, reflected and refracted electric fields, respectively. Each electric field can be represented by the follow equations:

$$\mathbf{E}_i(\mathbf{r}, t) = \mathbf{E}_{0i} e^{i(k_i \mathbf{r} - \omega_i t)} \quad (2.34)$$

$$\mathbf{E}_r(\mathbf{r}, t) = \mathbf{E}_{0r} e^{i(\mathbf{k}_r \mathbf{r} - \omega_r t + \varepsilon_r)} \quad (2.35)$$

$$\mathbf{E}_t(\mathbf{r}, t) = \mathbf{E}_{0t} e^{i(\mathbf{k}_t \mathbf{r} - \omega_t t + \varepsilon_t)} \quad (2.36)$$

where ε_r and ε_t are the phase constants if the position of the origin is not unique. However, the boundary conditions must be satisfied at all times for all points along the boundary. Thus at any point on the boundary, all waves, incident, reflected and refracted must have the frequency and phase

$$\omega_i = \omega_r = \omega_t \quad (2.36)$$

and the ε_r and ε_t terms disappear. The phase of a wave can be given by

$$\mathbf{k} \cdot \mathbf{r} \quad (2.38)$$

and thus we have

$$\mathbf{k}_i \cdot \mathbf{r} = \mathbf{k}_r \cdot \mathbf{r} = \mathbf{k}_t \cdot \mathbf{r} \quad (2.39)$$

The propagation vector \mathbf{k} can be broken down as a combination of its x , y , and z axis components. In Figure 2.4, for each of the incident, reflected, and refracted wave vectors, $z = 0$ since \mathbf{k} is two-component vector lying in the x - y plane. At a point along the boundary, $y = 0$, thus

$$\mathbf{r} = (x, 0, 0) \quad (2.40)$$

This leaves only the horizontal x -component as the only non-zero value and we have

$$\mathbf{k}_i = k_i (\sin \theta_i \hat{\mathbf{x}} + 0 \hat{\mathbf{y}} + 0 \hat{\mathbf{z}}) \quad (2.41)$$

$$\mathbf{k}_r = k_r (\sin \theta_r \hat{\mathbf{x}} + 0 \hat{\mathbf{y}} + 0 \hat{\mathbf{z}}) \quad (2.42)$$

$$\mathbf{k}_t = k_t (\sin \theta_t \hat{\mathbf{x}} + 0 \hat{\mathbf{y}} + 0 \hat{\mathbf{z}}) \quad (2.43)$$

Combined with Eq. (2.39), at the boundary for all points and values of time,

$$k_i \sin \theta_i = k_r \sin \theta_r = k_t \sin \theta_t \quad (2.44)$$

Since the incident and refractive waves propagate in the same medium, the wave vectors are the same, therefore the incident and reflected angles are equal. This leads to Snell's first law.

$$\theta_i = \theta_r \quad (2.45)$$

If $k = n/c$, then Eq. (2.44) can be expressed as Snell's second law:

$$n_1 \sin \theta_i = n_2 \sin \theta_t \quad (2.46)$$

The amplitudes of the reflected and refracted waves from the incident wave are given by the Fresnel equations. For electric fields perpendicular to the plane of incidence, s -polarization,

$$r_s = \frac{E_{0rs}}{E_{0is}} = \frac{n_i \cos \theta_i - n_t \cos \theta_t}{n_i \cos \theta_i + n_t \cos \theta_t} \quad (2.47)$$

$$t_s = \frac{E_{0ts}}{E_{0is}} = \frac{2n_i \cos \theta_i}{n_i \cos \theta_i + n_t \cos \theta_t} \quad (2.48)$$

where r and s are the reflected and refracted amplitude coefficients respectively, and the s subscript denotes s -polarization.

For electric fields parallel to the plane of incidence, p -polarization,

$$r_p = \frac{E_{0rp}}{E_{0ip}} = \frac{n_t \cos \theta_i - n_i \cos \theta_t}{n_i \cos \theta_t + n_t \cos \theta_i} \quad (2.49)$$

$$t_s = \frac{E_{0tp}}{E_{0ip}} = \frac{2n_i \cos \theta_i}{n_i \cos \theta_t + n_t \cos \theta_i} \quad (2.50)$$

where the p subscript denotes p -polarization.

Further simplification can be made using Snell's Law, whereupon the Fresnel equations become the commonly seen

$$r_s = \frac{E_{0rs}}{E_{0is}} = -\frac{\sin(\theta_i - \theta_t)}{\sin(\theta_i + \theta_t)} \quad (2.51)$$

$$r_p = \frac{E_{0rp}}{E_{0ip}} = \frac{\tan(\theta_i - \theta_t)}{\tan(\theta_i + \theta_t)} \quad (2.52)$$

$$t_s = \frac{E_{0ts}}{E_{0is}} = \frac{2 \sin \theta_t \cos \theta_i}{\sin(\theta_i + \theta_t)} \quad (2.53)$$

$$t_p = \frac{E_{0tp}}{E_{0ip}} = \frac{2 \sin \theta_t \cos \theta_i}{\sin(\theta_i + \theta_t) \cos(\theta_i - \theta_t)} \quad (2.54)$$

The reflectance is the intensity ratio of reflected light to the incident light, and is proportional to the amplitudes squared.

$$R_s = |r_s|^2 = \left| \frac{E_{0rs}}{E_{0is}} \right|^2 \quad (2.55)$$

$$R_p = |r_p|^2 = \left| \frac{E_{0rp}}{E_{0ip}} \right|^2 \quad (2.56)$$

The reflectance is dependent on the angle of incidence and the polarization of light, as shown by Eqs. (2.55) and (2.56).

2.2.4 Brewster Angle

At a specific angle, the fraction of reflected p -component approaches 0. From Eq. (2.52), it can be seen that this happens when $\theta_i + \theta_t = 90^\circ$, where the denominator tan

(90°) reaches to infinity. This angle of incidence θ_i is known as the Brewster angle, θ_B and can be calculated from Snell's law of refraction:

$$n_1 \sin \theta_i = n_2 \sin(90 - \theta_i) = n_2 \cos(\theta_i) \quad (2.57)$$

$$\frac{n_2}{n_1} = \frac{\sin(\theta_i)}{\cos(\theta_i)} = \tan(\theta_i) \quad (2.58)$$

$$\theta_B = \theta_i = \tan^{-1}\left(\frac{n_2}{n_1}\right) \quad (2.59)$$

For an air-water interface, the refractive indices are 1 and 1.33, respectively. The Brewster angle therefore is 53.1°.

2.2.5 Factors for Intensity of Light

At the Brewster angle, the *p*-polarized reflectance is near 0 ($\leq 10^{-8}$). In an ideal situation, the interface has infinitely thin and smooth, and thus there is an immediate change in refractive index going from one medium to the other. However, for a real interface, the surface is rough, and the refractive indices do not change abruptly, thus the reflectance is slightly higher. Reflectance is also affected by interfacial properties such as the thickness, density, and optical anisotropy. However, monolayers adsorbed at the air-water interface can still be studied as the refractive index of the monolayer is different from that of air or water, and there is a significant increase in reflectance off the monolayer. This difference in intensity from the reflected light is used as an imaging contrast to form the BAM images.

Chapter 3: Material and Methods

3.1 Materials

DPPA (sodium salt) as lyophilized powder was purchased from Avanti Polar Lipids, Inc. with a purity of >99% and used without purification. LPS purified by phenol extraction and by trichloroacetic acid (TCA) extraction were purchased from Sigma-Aldrich. ACS certified grade salts NaCl, KCl, MgCl₂, CaCl₂, and MgSO₄ with purities >99% were purchased from Fisher Scientific. Synthetic sea salt (Instant Ocean®) was purchased commercially. Chemical composition and ion concentrations of the synthetic sea salt are found in Table 3.1. Chloroform and methanol solvents of HPLC grade were purchased from Fisher Scientific. Trace metal grade HCl acid and NaOH base were purchased from Fisher Scientific. Monolayers were spread on a pure water subphase with a resistivity of 18.0 MΩ·cm purified by a Barnstead nanopure filtration system, and a measured pH of 5.6. All experiments were performed at room temperature (22 ± 1 °C) and atmospheric pressure.

3.2 Methods

3.2.1 Sample Preparation

Stock solutions of DPPA were prepared by dissolution of lyophilized DPPA powder in a chloroform/methanol mixture with a 3:1 (v/v) ratio. DPPA (sodium salt) has a molecular weight (M_w) of 670.873 g/mol; the average M_w of Avanti DPPA-Na provided is 670.455 g/mol due to variability in Na⁺. Stock solutions of LPS were dissolved in pure

water. The structure of LPS varies in the core section, Lipid A, and O-antigen chain, as well as the number of repeating units. Since LPS is heterogeneous and forms aggregates, molecular masses over 1 million Da can occur. When treated with sodium dodecyl sulfate (SDS), a range of ~50-100 kDa is reported.⁷¹ Due to this variability, the molar concentration of LPS cannot be determined, and instead is reported in units of mg/mL for sample preparation. NaCl, KCl and MgSO₄ salts were baked in crucibles at 650°C to remove any organic contaminants.⁷² All aqueous salt solutions were prepared by dissolution in pure water. MgCl₂ and CaCl₂ solutions were filtered at least thrice using activated carbon filters (Whatman Carbon-Cap 75, Fisher Scientific, Pittsburgh, PA, USA) to remove any organic contaminants.⁷² Further testing by Ellen M. Adams indicated absence of organic contaminants by vibrational sum frequency generation (VSFG) spectroscopy taken in the surfactant CH stretching region (2800-3000 cm⁻¹). The concentration of these stock solutions was standardized by the Mohr titration technique.⁷³ Artificial sea water (ASW) was prepared by dissolution of Instant Ocean[®] sea salt in accordance with manufacturer specifications. Custom made artificial sea water was prepared by mixing prepared stock solutions of NaCl, KCl, MgCl₂, CaCl₂, and MgSO₄, to equal concentrations found in Instant Ocean[®]. Serial dilution of stock solutions was used to prepare subphases. The pH of prepared solutions was not found to vary significantly from that of pure water. (pH 5.6 ± 0.5). pH regulation of solutions was done by adding concentrated HCl and 10 M NaOH dropwise to the prepared solution.

Table 3.1 Chemical composition and ion concentration of Instant Ocean[®] synthetic sea salt.

Ion	Concentration (g/kg Water)	Concentration (mol/L)
Na ⁺	10.780	0.4521
K ⁺	0.420	0.0104
Mg ²⁺	1.320	0.0530
Ca ²⁺	0.4	0.0096
Sr ²⁺	0.0088	9.64×10^{-5}
Cl ⁻	19.290	0.5315
SO ₄ ²⁻	2.660	0.0267
HCO ₃ ⁻	0.200	0.0032
Br ⁻	0.056	6.75×10^{-4}
F ⁻	0.001	5.11×10^{-5}

3.2.2 Π -A Isotherms

Π -A isotherms were obtained using a KSV Minitrough (KSV Instruments, Finland). The trough is made of Teflon and has dimensions of 168 mm \times 85 mm. The monolayer is symmetrically compressed using two barriers coated with Delrin, a hydrophilic material. Surface pressure (SP) and mean molecular area (MMA) were measured during compression by the Wilhelmy plate method. Filter paper (Ashless grade, Whatman) was used as Wilhelmy plates. Prior to each experiment, the trough was rinsed several times with nanopure water, then filled. Presence of impurities was checked by sweeping the subphase with the barriers and observing no significant change in the surface pressure (<0.1 mN/m). A measured amount of lipid or LPS solution was spread dropwise on the subphase using a microsyringe (Hamilton, 250 μ L). After spreading, solvent evaporation was allowed for 11 min after spreading. The barriers were compressed at a rate of 5 mm/min/barrier.

3.2.3 BAM Images

BAM images were simultaneously measured with Π -A isotherms on a custom-built setup by Ellen Adams and Zishuai Huang. The setup consists of a goniometer to which all other components are mounted on, a laboratory jack sample stage, and a black Plexiglass box enclosure to block ambient light, dust, and airflow. Attached to the goniometer are two arms: the left arm supports the optical emission components, such as the laser source, half-wave plate (HWP) and a polarizer. The right arm supports the optical detection components, which include the objective lens, a tube lens, and a charge-coupled device (CCD) camera. Further optical component details are discussed in the following section. The goniometer controls the incident angle of the arms, which can be varied from 40-60°. For the BAM images shown, the incident angle is set to near that of the Brewster angle of water (53.1°). The Langmuir trough sits on the vertically adjustable laboratory jack, and a flat black glass plate sits upon a Teflon wedge at the bottom of the trough. The plate is inclined to absorb refracted light from hitting the detector. Images are cropped from the full 800 $\mu\text{m} \times 800 \mu\text{m}$ resolution to 600 $\mu\text{m} \times 600 \mu\text{m}$ from the center. No further image processing was done outside the ANDOR BAM imaging program.

Laser Source

A HeNe laser (Research Electro-Optics) is used as the light source. The laser emits highly *p*-polarized light (>500:1) at 543 nm with a maximum output power of 5 mW.

Half-Wave Plate and Polarizer

The output light from the laser source is first attenuated by a HWP (Ekspla, Lithuania) with an anti-reflective coating at 532 nm. Further filtration of the output light is done by a Glan prism (Ekspla, diameter 14 mm) with a coating that is antireflective in the range 430-960 nm.

Objective Lens and Tube Lens

An infinity-corrected Nikon CF super-long working distance objective lens is used in this BAM setup. It has a linear magnification of 10 \times , a working distance of 20.3 mm, and a numerical aperture of 0.21. The objective lens is mounted on two micrometer stages so that the x and y axes can be adjusted accordingly. Along with the objective lens is a tube lens (MXA22018, Nikon) with a focal length of 200 mm. The tube lens focuses the collimated light from the objective lens into the CCD.

CCD Camera

BAM images were captured on a back-illuminated electron multiplying CCD camera (DV887-BV, Andor Technology). The CCD has 512 \times 512 active pixels. Each pixel has a size of 16 μm \times 16 μm resulting in a total image area of 8.2 mm \times 8.2 mm. Andor Solis software along with a CCI-22 PCI controller card were used for image acquisition. 14 bit megapixel images were recorded with pixel read out rates of 10, 5, 3, or 1 MHz.

Chapter 4: Results and Discussion

4.1 Surface Pressure Isotherms

4.1.1 Phase behavior of DPPA on water

Π -A isotherms show the phase behavior of DPPA monolayers. Figure 4.4 shows the Π -A isotherm of DPPA on nanopure water. For DPPA, a liftoff in the isotherm is observed, followed by a kink in the slope which then levels off. Depending on factors such as small temperature variations and differences in spreading technique, the liftoff point can range from a sharp liftoff to a more gradual curvature. To determine the liftoff point, the slope of the first phase transition is extrapolated in a straight line to where $\Pi = 0$ mN/m, and the MMA of the liftoff obtained from that point.

The phase behavior of DPPA and its interactions with various proteins and other compounds has been documented before.^{34, 74-77} However, the literature reported values of DPPA liftoff vary greatly. As seen in Figure 4.5, a consensus has not been reached. Sources of variation can include the purity of DPPA depending on the source, and cleanliness of the experimental procedure.

To the author's best knowledge, the current measured data is valid due to careful cleaning procedure and averaging of all data between DPPA purchased from different sources: Sigma-Aldrich and Avanti Polar Lipids.

The pre-liftoff point of DPPA corresponds to a coexistence region between the LE and LC phases. In the LE phase, molecules are disordered and fluid-like, compared to the

more ordered and tightly packed LC phase. The absence of a distinct LE phase in DPPA indicates that strong attractive forces exist that inhibit the DPPA molecules from acting fluid-like as those found in the LE phase. One explanation is the relative small size of the phosphate headgroup compared to alkyl tails, allowing the van der Waals forces and hydrophobic interactions to dominate.⁷⁷ This is reflected by the high phase transition temperature of DPPA (67°C). The phase transition temperature is where lipids change from an ordered gel phase below the transition temperature to a disordered liquid crystalline phase above the transition temperature. Studies have shown increasing alkyl chain lengths correlate to higher phase transition temperatures due to the increase in hydrophobic interactions.⁷⁸ At above the phase transition temperature, the disordered liquid-crystalline phase can cause the appearance of the LE phase.⁷⁹ DPPA thus exists as a highly ordered gel phase, preventing the appearance of a LE phase at room temperature.

Monolayer studies of similar lipids such as DPPE, and DPPS, and DPPG can also display an absence of a LE phase below their phase transition temperatures.⁷⁹⁻⁸¹ This trend can be correlated to the effect of headgroups on the phase transition temperatures, although it is considered secondary to the alkyl chain interactions. An increased attraction between headgroups increases the phase transition temperature. DPPE, DPPS and DPPG all engage in some degree of hydrogen bonding, and have phase transition temperatures above room temperature (63, 54, and 41°C, respectively). However, they also have larger headgroups, resulting in repulsive steric interactions. In addition, DPPS and DPPG are anionic and may have additional electrostatic repulsions due to their negative headgroup charges. Thus DPPA with its small headgroup and highest phase transition temperature can display strong hydrogen bonding without any opposing repulsive effects,

Liftoff of the DPPA isotherm at approximately $37.3 \text{ \AA}^2/\text{molecule}$ indicates a transition to LC phase based on the abrupt change in slope of the isotherm. This is also seen in the BAM images. A kink appears at $34.2 \text{ \AA}^2/\text{molecule}$, where the observed sharp change in slope indicates a second-order phase transition from a TC phase to an UC phase. This second slope has been attributed to a solid phase rather than UC phase due to its low compressibility.⁸² However, X-ray diffraction studies indicate that DPPA goes from an oblique to rectangular to hexagonal packing lattice as the monolayer is compressed.⁸³ Hexagonal packing is the densest packing order and has been attributed to intermolecular hydrogen bonding for lipids.⁸⁴

At about 46 mN/m , the isotherm plateaus indicating a constant pressure collapse. The collapse mechanism, although poorly understood, is believed to be due to folding and sliding of the monolayer for a constant-pressure collapse.

4.1.2 Effect of pH and ionization on the phase behavior of DPPA on water

The speciation curves of the DPPA phosphate headgroup are shown in Figure 4.6. DPPA has a $\text{pK}_1 \sim 3.8$ and a $\text{pK}_2 \sim 8.5$.⁸⁵⁻⁸⁶ Between pH 3.8 and 8.4, the phosphate headgroup carries one negative charge, as only one of the two available oxygen atoms are protonated. This includes the pH of nanopure water (5.6), physiological pH (7.4), and ocean pH (~ 8). Below pH 3.8, the neutral species dominate, where DPPA is fully protonated. Above pH 8.5, DPPA is dominated by the doubly negatively charged species DP-PO_4^{2-} where both oxygens are completely deprotonated. Although the DPPA is primarily in the DP-HPO_4^- species for the studied systems of interest, understanding of its interactions at various ionization states is necessary for insight into forces driving

monolayer formation of DPPA. DPPA can be induced into the -2 state via the electrostatic-hydrogen bond switch.⁵³ In addition, the pH of some atmospheric aerosols can drop to well below 2, particularly sulfuric acid aerosols, which would result in formation of the neutral species DP-H₂PO₄.⁸⁷

Figure 4.7 shows the isotherms of DPPA monolayers on nanopure water at various pH. Immediately noticeable is the isotherm at basic pH 10.3. The lift off area is expanded from 37.3 to 41.5 Å²/molecule, which can be explained by the increased electrostatic repulsion from the negative charges on PO₄²⁻ headgroup. Presence of the TC phase disappears, as the DPPA is not able to pack tightly enough where the tails are forced perpendicular for very long before the onset of the collapse phase. The isotherm surface displays an increased surface pressure as well as collapse pressure, indicating increasing stability of the monolayer to stay as a monolayer before collapsing into 3D structures. This is due to nature of repulsive electrostatic interactions opposing the surface tension which is a measure of the excess attractive forces the molecules feel towards each other at the surface.

At acidic pH 1.7, the monolayer does not display any significant change in MMA. This contradicts a previous study which observed a small condensing effect at lower pH.⁸² The phosphate headgroup carries no charge, and the decrease in electrostatic repulsion should allow a tighter possible packing of the DPPA molecules, and thus a lower lift off area. However, this is not seen, although the isotherms display slight differences, this is due to magnification of the isotherm. The liftoff areas at pH 5.6 and 1.7 are 37.3 and 37.5 Å²/molecule, respectively, less than the 0.5 Å²/molecule margin of error. The TC-UC phase transition area also does not significantly change; 34.2 vs. 34.7

$\text{\AA}^2/\text{molecule}$. However, a decrease in the surface pressure of the phase transition is noted, from 22 to 16 mN/m. This decrease can indicate a slightly lower stability of the monolayer but the collapse pressure remains the same, which shows an acidic pH does not significantly affect the stability of DPPA monolayers.

The difference between observed results and previously reported results can be reconciled by hydrogen bonding. At very acidic pHs, the hydrogen bonding network of DPPA, both intramolecular and water-mediated is disrupted, although not to the same degree as that of very basic pHs.⁸⁴ A fully protonated phosphate headgroup has less ideal hydrogen bond formation than that of a partially protonated phosphate. This decrease in attractive hydrogen bonding along with a simultaneous decrease in repulsive electrostatic interactions can cancel out resulting in no significant change in the mean molecular area. The isotherms of DPPA on nanopure water at pH 5.6 and 8.0 also show no significant difference, as the liftoff areas are 37.3 and 36.8 $\text{\AA}^2/\text{molecule}$. Their phase transition surface pressure also displays a minor decrease from 22 to 20 mN/m. This can also indicate a slightly less stable monolayer, however the collapse pressure is also the same. At pH 8.0, the majority of the phosphate headgroups (~75%) still exist as PO_4^{2-} . This can explain why the isotherms are barely changed.

4.1.3 Effect of monovalent cations on the phase behavior of DPPA

DPPA monolayers on salt subphases exhibit different phase behavior compared to that on nanopure water due to headgroup interactions with the ions. Although phosphatidic acid monolayers under the influence of ions have been studied by MD

simulations, experimental Π -A isotherms of DPPA on salt solutions have been poorly studied.⁸⁸

Figure 4.8 shows the Π -A isotherm of DPPA on NaCl solutions of varying concentrations. A saturation effect is observed, as isotherms of concentrations ≥ 0.05 M are identical. To further identify the minimum saturation concentration, DPPA isotherms on 0.0025, 0.005, 0.02, 0.03, 0.04, 0.05 and 0.15 M NaCl solutions were plotted as a function of the concentration versus the mean molecular area corresponding to a surface pressure of 10 mN/m in Figure 4.9. An exponential fit was found to best model the experimental data and saturation does primarily occur at 0.05 M.

The NaCl concentration studies show that for the relevant DPPA systems of interest, the binding sites of DPPA for Na^+ are fully occupied. The ocean has a Na^+ concentration of around ~ 0.47 M,²⁹ while physiological concentrations of Na^+ are around 0.15 M. Both are well above the saturation concentration of 0.05 M Na^+ which rules out the possibility of incomplete binding. For the sake of simplicity, from this point on, discussion of the effects of all salt subphases on DPPA will only be for salt concentrations in the saturation regime to eliminate the impact of incomplete binding. We neglect the presence of Cl^- ions as studies have shown interact with lipids at the surface.⁸⁹ In addition, the negative charge of DPPA would inhibit the accumulation of anions at the surface.

Addition of NaCl to the water subphase results an expansion of the monolayer as well as a higher observed surface pressure. However, a higher collapse pressure is still observed corresponding to higher salt concentrations. This indicates the stabilizing effect of Na^+ ions on the DPPA monolayer, which will be further discussed in detail.

The liftoff area of DPPA in saturated NaCl solutions ≥ 0.05 M is expanded from 37.5 to 41.5 $\text{\AA}^2/\text{molecule}$. The second order phase transition from TC to UC phases observed in that of DPPA on nanopure water is still present but also occurs at larger mean molecular areas: 34 and 35.2 $\text{\AA}^2/\text{molecule}$ for water and NaCl subphases, respectively. The surface pressure at which the transition occurs is drastically increased from 22 to ~ 34 mN/m. A higher collapse pressure is also observed. The increase in MMA and surface pressure of the DPPA monolayer due to the presence of Na^+ cations indicates increased repulsive interactions countering the attractive van der Waals and hydrogen bonding and a stabilization of the monolayer.

A similar expansion trend is seen in DPPA monolayers on KCl subphases, as shown by Figure 4.9. DPPA is seen to saturate with K^+ cations at concentrations above 0.15 M KCl. However, there is not enough data to determine the saturation point. Ocean and physiological concentrations of K^+ are 0.01 and 0.005 M, respectively. While 0.01 M is estimated to be within saturation, a more comprehensive KCl saturation study is required.

The liftoff area of DPPA in saturated KCl solution is expanded from 37.5 to 40.5 $\text{\AA}^2/\text{molecule}$. The increase in MMA of the phase transition from TC to UC phase is similar to that of Na^+ (34 to 35.5 mN/m), while the surface pressure increases from 22 to 25 mN/m.

A comparison of the effects of the monovalent salts is shown in Figure 4.10. Both monovalent salts expand and stabilize the DPPA monolayer, however the expansion effect of Na^+ is greater than that of K^+ , despite its smaller size. The isotherms for both

salt subphases converge indicating the cations are partially squeezed out of the monolayer to a certain degree.

The larger effect of Na^+ on DPPA monolayer expansion can be explained by several possible factors. MD simulations of monovalent ions on DPPA and other phospholipids have indicated differences in binding affinity to the carbonyl and phosphate groups.⁹⁰ Early MD studies reported preferential binding of Na^+ to the carbonyl group while K^+ preferred binding to the phosphate.⁹¹⁻⁹³ Later studies with different force fields indicated binding primarily occurs at the phosphate headgroup, and a very weak binding by potassium.⁸⁹ Thus the reliability of MD simulations is limited due to the force field dependency. However, it is most likely both cations bind primarily to the phosphate, with minor secondary binding of Na^+ to the carbonyl group.

Table 4.1 Bare and hydrated ionic radii and their associated Gibbs free energy of hydration (calculated and experimental).⁹⁴

Ion	Ionic radius (Å)	Hydrated radius (Å)	G_{calc} (kJ/mol)	G_{exp} (kJ/mol)
Na^+	1.02	2.18	-385	-365
K^+	1.38	2.12	-305	-295
H_2PO_4^-	2	2.33	-245	-465
CH_3CO_2^-	1.62	2.17	-300	-365

The ability of Na^+ to penetrate further into the monolayer to bind to the carbonyl group can be explained by the smaller ionic radii of Na^+ as well as its Gibbs free energy of hydration. Table 4.1 gives the values of the ionic radii, hydrated radii and Gibbs free energy of hydration. In aqueous solutions, cations are surrounded by water molecules, and this solvation shell increases the effective radius. However, both Na^+ and K^+ have

relatively low free energies of hydration, allowing them to lose water molecules from the solvation shell easily. Other lipid studies have also reported deprotonation and dehydration steps involved in the binding of cations to headgroups.^{31, 95} Na^+ and CH_3CO_2^- display similar free energies of hydration, and this may be a factor in the preferential binding of Na^+ to the carbonyl group. The weakness of this explanation is that the CH_3CO_2^- anion is acting as a proxy for the carbonyl moiety of DPPA. While the carbonyl carries some negative charge, it is not the same as a free carboxylic acid group with a free negative charge.

If the Na^+ cations are indeed found deeper in the lipid region, steric interactions of the cation with the inner core of DPPA may prevent DPPA from packing as tightly as that on neat water. Evidence to support this is shown from the isotherms in Figure 4.11: as the lipid monolayer is compressed, the isotherms for both salt subphases converge to the same mean molecular areas and surface pressures in the UC phase. This converging phase behavior is typically attributed to a squeezing out effect, where Na^+ cations are physically expelled from the monolayer, leaving interactions to reside primarily with the phosphate headgroup closer to water region instead of the carbonyl in the hydrophobic deep lipid region. This also supports phosphate being the primary binding site for both ions.

Another proposed explanation for the preferential binding of cations to different anions is the “law of matching water affinities”, as proposed by Collins.⁹⁶ In simple terms, it can be described as “small cations bind preferentially with small anions or anionic groups of similar energy and vice versa.” Binding between ions is affected by the relative strength of their ion-water water interactions compared to the water-water

interactions. When small strongly hydrated hard ions meet, they experience strong electrostatic attractions due to their high charge densities. Thus, they can form inner sphere pairs where water molecules are expelled between the ions. Likewise, for large soft ions of opposite charge, the solvation shell is loosely bound so they too can expel water molecules and undergo inner-sphere binding. However, when small hard ions meet large soft ions, they undergo outer-sphere binding, or solvent-mediated binding where a water molecule separates the two ions. Thus the inability of mismatched ions to form strong inner-sphere ion pairs explains the difference in binding of different cations to the same anion. Na^+ is closer in size to carboxylate (carbonyl proxy) than K^+ , while both are similar to phosphate.

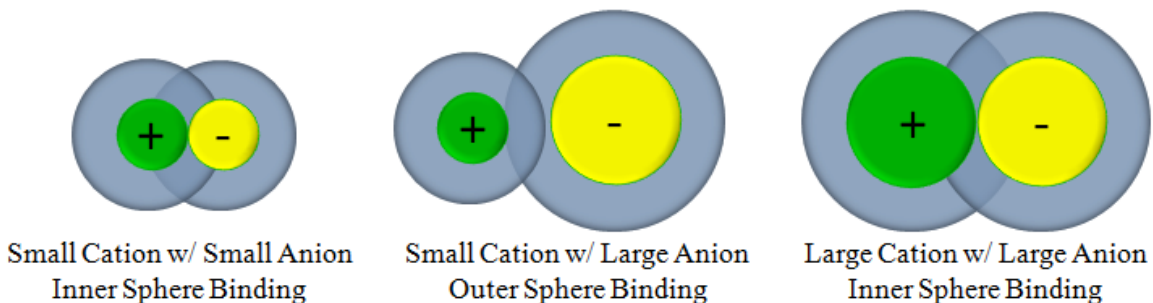


Figure 5 Visual representation of law of matching water affinities.

While Collin's law of matching water affinities is empirically derived, it has been supported by MD simulations. Jungwirth et al. calculated the change in free energy of swapping an anion pair with potassium for sodium.⁹⁷ A decrease in free energy was found for carboxylate anionic group, while the singly charged anionic phosphate group displayed little change, and thus no preference.

Finally, the argument of the significance of water structure can glean insight into the differences between Na^+ and K^+ . Preceding Collin's law is the Hofmeister series,

which is a classification of order of ions to salt in or salt out proteins, worked out by Franz Hofmeister. However, the protein effects are beyond the scope of this discussion. More importantly, the Hofmeister series is believed to be related to the trend of ions to act as kosmotrope or chaotrope, although some studies have found no straightforward correlation.⁹⁸ The term kosmotrope means order-making, and kosmotropes are defined by their ability to contribute to the stability of water, and by extension hydrogen bonding.⁹⁹ Kosmotropes are typically small ions or ions with high charge densities such as Mg^{2+} , which orient the neighboring oxygen atoms of water molecule towards themselves. Chaotropes on the other hand means order-breaking, and they destabilize the water structure and hydrogen bonding network.⁹⁹ Chaotropes are typically large ions with low charge densities such as iodide.

However, this term of structure-maker and structure-breaker can be misleading: kosmotropes stabilize and increase the local hydrogen bonding network primarily in the direct vicinity of the ion: it would be more accurate to describe them as local water structure-makers. The same applies to chaotropes, the effects on water structure are in the immediate region surrounding the ions. According to Marcus, Ca^{2+} , Mg^{2+} are chaotropes, Na^+ is a borderline chaotrope, while K^+ is a kosmotrope.⁹⁹

If we attribute hydrogen bonding as the major force in the monolayer formation of DPPA, then the effect of cations on the water hydrogen bonding network would indeed affect the monolayer properties as seen in the isotherms. With Na^+ ions bound to DPPA, the water molecules arrange themselves around the bound sodium stabilizing the local water structure. However, the hydrogen bonds of the adjacent water molecules among themselves as well as between the phosphate headgroups are disrupted in favor of

forming even stronger hydrogen bonds in the vicinity of the Na^+ ion. Thus a “structure-making” ion like Na^+ causes structure breaking when viewed from another perspective. Compared to a weak kosmotrope like K^+ , which would not affect water molecules in the vicinity as strongly as Na^+ , increased disruption of the hydrogen bonding forces between DPPA could explain why Na^+ expands the monolayer further than K^+ .

4.1.4 Effect of monovalent cations on the phase behavior of DPPA at low and high pH

A comparison of cation binding at the various ionization states of DPPA can shed further light on the binding affinity of Na^+ vs. K^+ . Figure 4.12 shows the Π -A isotherm of DPPA on NaCl and KCl subphases at acidic conditions. The isotherm of DPPA on NaCl at pH 2.5 shows a very minor expansion of the monolayer. The liftoff area is increased by $\sim 1 \text{ \AA}^2/\text{molecule}$ while the phase transition area and surface pressure remain the same. This extremely small change in the isotherm indicates very weak binding of sodium to DPPA when phosphate headgroups are fully protonated. Earlier studies by the Allen group on the binding of Na^+ and K^+ cations to the carboxylic group of PA monolayers have shown a two-step binding process: deprotonation of the headgroup followed by binding of the cation.³¹⁻³³ The same mechanism appears to be the case with cations with the phosphate headgroup, however, the low pH of the subphase inhibits deprotonation of the headgroup, preventing Na^+ from binding competitively with H^+ to DPPA. However, an alternative explanation would be the ability of Na^+ to interact with the carbonyl groups while the phosphate groups are completely unreactive.

In comparison to Na^+ , the isotherm of DPPA on KCl at acidic pH 2.6 shows no change from that on neat water. This clearly shows no binding of K^+ cations to DPPA at all. From these differences, the binding affinity of Na^+ and K^+ to DPPA can be distinguished, in favor of Na^+ . This could be explained again by the increased affinity of Na^+ to bind with the phosphate group, due to the law of matching water affinities, Na^+ is smaller than K^+ and has a higher charge density, thus it is able to disrupt the hydrogen bonding network more, allowing easier de-protonation of the phosphate and subsequent binding. However, all isotherms converge, indicating expulsion of all ions from the DPPA monolayer at a high compression area. This can indicate the Na-PO_4 bond is still very weak under very acidic conditions and Na^+ is eventually expelled from the monolayer in favor of protonation. However, the alternative argument still remains valid, as a fully protonated headgroup could prevent both cations from binding to phosphate but not the Na^+ from binding to carbonyl. Upon further compression of the monolayer, the Na^+ is squeezed out, and the isotherm reverts back to that of DPPA on neat water.

Figure 4.13 shows the Π -A isotherm of DPPA on NaCl and KCl subphases under very basic conditions. The isotherms for both salt subphases at pH 10.1 both show disappearance of the TC-UC phase transition and are extremely expanded compared to that of isotherms at pH 5.6. The liftoff point is a curved slope with no distinguishing features, however, NaCl is slightly further expanded by $\sim 1 \text{ \AA}^2/\text{molecule}$. A simple electrostatic treatment of cation binding with a highly negatively charged headgroup predicts a condensing effect on the monolayer due to electrostatic screening of the charges by the cations, which has been reported in MD simulations.¹⁰⁰ However instead of seeing salt isotherms at a lower MMA than that of neat water at pH ~ 10 , both NaCl

and KCl are extremely expanded ($\Delta A > 5 \text{ \AA}^2/\text{molecule}$). This can be explained by counter-ion cloud repulsion, where the -2 charge draws the cations to the surface, similar to an electrical double-layer. The formation of cation “clouds” around the phosphate headgroup and accumulation of positive charges results in high electrostatic repulsion causing great expansion of the DPPA monolayer. In addition, the collapse pressures of DPPA on both salt solutions are noticeably higher than that of on neat water. This indicates a very tight binding of the cations to the monolayer, preventing squeeze out and stabilizing the monolayer. The same trend of increased binding affinity of Na^+ to K^+ is also present as the Na^+ exhibits a higher collapse pressure.

4.1.5 Effect of divalent cations on the phase behavior of DPPA

While the effect of monovalent cations on DPPA monolayers has been investigated, there is greater interest in the effect of divalent cations for both biological and atmospheric studies. Figure 4.15 shows the Π -A isotherms of DPPA on 0.15 and 0.6 M CaCl_2 subphase. Both isotherms do not display any significant difference, indicating the saturation point of CaCl_2 for DPPA has already been reached. Further experiments are needed to explore the saturation regime of CaCl_2 as typical concentrations of Ca^{2+} in ocean and physiological conditions are found in the μM range.²⁹

The liftoff area of the CaCl_2 occurs at $\sim 39 \text{ \AA}^2/\text{molecule}$, with the phase transition at $35 \text{ \AA}^2/\text{molecule}$ occurring at 22 mN/m. This shows a slight expansion effect of Ca^{2+} on the DPPA monolayer, as well as increased stability from the higher collapse pressure.

A similar effect is also seen in the Π -A isotherm of MgCl_2 , shown in Figure 4.14. Mg^{2+} also displays an expansion of the DPPA monolayer, with 0.15 and 0.6 M in the

saturation regime. As with CaCl_2 , further saturation studies are needed as typical ocean and physiological concentrations are also in the μM range. MgCl_2 displays a liftoff area at $41.5 \text{ \AA}^2/\text{molecule}$, and a curved LC phase making identification of a phase transition difficult. However, a phase transition appears to be at $\sim 35 \text{ \AA}^2/\text{molecule}$ at a surface pressure of $\sim 35 \text{ mN/m}$. As with calcium, an expansion and stabilization of the monolayer due to higher collapse pressures is observed.

Figure 4.16 shows the comparison between the isotherms of Ca^{2+} and Mg^{2+} . The effects of divalent ions on lipid monolayers have a critical importance in biology and have been documented in other studies. Both Ca^{2+} and Mg^{2+} expand the DPPA although it is clear that Mg^{2+} expands the monolayer more than Ca^{2+} . In both cases, just like the monovalent cations, they are physical inserting themselves into the lipid monolayer; Ca^{2+} has been found to expand DPPC monolayers by $4 \text{ \AA}^2/\text{lipid}$ which is exactly its ion cross sectional area.¹⁰¹ However, Ca^{2+} only expands the DPPA monolayer by $1 \text{ \AA}^2/\text{lipid}$ which indicates other attractive forces are in effect to oppose the steric repulsion. It has been noted the +2 charge on divalent cations in general are able to bridge and bind two lipids, as well as ordering them.¹⁰¹ In addition to bridging lipid headgroups, the divalent cations can more efficiently screen negative headgroup charges than monovalent cations at twice the rate.

Divalents in general, especially Ca^{2+} , have been found to bind strongly with phosphatidic acid even at low micromolar concentrations.¹⁰² MD simulations have suggested different preferential binding sites in negatively charged phospholipids for Ca^{2+} and Mg^{2+} , such as the carbonyl and phosphate oxygens.¹⁰³⁻¹⁰⁴ Spectroscopic evidence on the shifts of the carbonyl and phosphate bands of 1-palmitoyl-2-

oleoylphosphatidylcholine (POPC) have indeed indicated differences between Ca^{2+} and Mg^{2+} , with stronger shifts in the carbonyl bands in the presence of Ca^{2+} .

Table 4.2 Bare and hydrated ionic radii and their associated Gibbs free energy of hydration (calculated and experimental).⁹⁴

Ion	Ionic radius (Å)	Hydrated radius (Å)	G_{calc} (kJ/mol)	G_{exp} (kJ/mol)
Mg^{2+}	0.72	2.99	-1940	-1830
Ca^{2+}	1	2.71	-1515	-1505
H_2PO_4^-	2	2.33	-245	-465
CH_3CO_2^-	1.62	2.17	-300	-365

According to Collins' law of matching water affinities, Ca^{2+} has a higher binding affinity to phosphate than Mg^{2+} and forms tight inner-sphere binding with phosphate. Mg^{2+} has more mismatch with phosphate, being a small hard cation. As seen in Table 4.2, Mg^{2+} has a large hydrated radius, and has a very low free energy of hydration, holding on its solvation shell tightly. Thus, Mg^{2+} forms outer-sphere solvent-separated bonds with the phosphate headgroup.

However, there is a seemingly contradictory trend of Ca^{2+} binding more strongly to DPPA yet expanding the monolayer less than Mg^{2+} . Part of the explanation can be made with sterics: Mg^{2+} retains an intact solvation shell due to its high charge density in addition to forming solvent-separated bonds. As seen in Table 4.2, although Mg^{2+} has a smaller ionic radius than Ca^{2+} , it has a larger hydrated radius. As Mg^{2+} retains more of its solvation shell than Ca^{2+} , the presence of additional water molecules would result in a larger mean lipid area.

The argument of water structure can also contribute to explaining why Mg^{2+} expands the DPPA monolayer more than Ca^{2+} . If we establish hydrogen bonding as the dominant force in DPPA monolayers, disruption of the network would result in an expanded monolayer. As in the example of Na^+ , chaotropes would disrupt the hydrogen bonding of DPPA in favor of their local hydrogen bonds and Mg^{2+} is a stronger chaotrope than Ca^{2+} .

4.1.6 Effect of surface-active contaminants on the phase behavior of DPPA

Previous studies done in the Allen group have shown that the cleanliness and purity of purchased salts is critical for measurements at surfaces. Surface tension is sensitive to surface-active organic contaminants, which are observed to increase the surface pressure. Hua et al. showed that ACS grade salts displayed different spectra from ACS ultrapure salts using VSFG spectroscopy.⁷² Thus the ACS grade salts used in this study contain organic contaminants that can affect the surface measurements. The presence of μM concentrations of divalent cations can also affect the measurements using monovalent salts leading to incorrect data. To eliminate organic contaminants, Hua et al. found that baking salts at 650°C for NaCl and KCl, and activated carbon filtration of MgCl_2 and CaCl_2 was sufficient to eliminate the presence of organics by comparing the treated salts with ultrahigh purity salts.

Figures 4.18-4.20 show the isotherms of DPPA on NaCl, MgCl_2 , CaCl_2 solutions at pH 5.6 for untreated and treated solutions. There is a noticeable difference in the isotherms on salt solutions made from ACS grade salts used as received compared to the salt solutions that were treated to remove organics. In particular, the isotherms have

higher MMAs, surface pressures, and lose information contained in the slopes and phase transitions. The untreated solutions also gave irreproducible isotherms, whereas upon treatment, the isotherms changed dramatically and were reproducible. Initial isotherm reproducibility issues in this study were resolved when subphases were cleaned and checked for organics. Preliminary treatments of monovalent salt solutions with ethylenediaminetetraacetic acid (EDTA) to determine the impact of divalent cations on isotherms with monovalent cations were inconclusive and thus not discussed in this thesis.

4.1.7 Phase behavior of DPPA on ASW

Figure 4.21 shows the Π -A isotherms of DPPA on ASW solutions. The Instant Ocean isotherm from commercially purchased Instant Ocean[®] salts show broad slopes and excessive monolayer expansion indicative of organic contamination. Thus to properly study the effects of multiple ions on DPPA monolayers such as that of sea water, custom-made artificial sea water solution prepared from clean salt stock solutions was needed. The blue isotherms labeled ASW NaCl and ASW 0.1X are DPPA monolayer isotherms prepared on ASW solutions at ocean concentrations and 0.1X ocean concentrations. There is no noticeable difference between the two isotherms indicating saturation.

The isotherms display an expansion of the monolayers, but between that of Na^+ which expanded DPPA the most, and Ca^{2+} which expanded the least. This indicates a non-linear combination of salts, with likely competitive binding of DPPA by the cations. Cations with higher binding affinities would be more likely to bind over cations with

lower affinities. To verify this, the concentration of Na^+ and K^+ were switched in the isotherm labeled ASW KCl. The majority of cations constituting ASW are Na^+ ions, yet switching the concentration a majority of K^+ ions did not noticeable change the isotherm. This indicates the divalent cations are more competitively binding for DPPA sites than the monovalent cations.

4.1.8 Comparison of salt effects on the phase behavior of DPPA

Figure 4.17 shows Π -A isotherms for all four salts for comparison. The effect of salts expanding the DPPA monolayer is ordered as follows: $\text{Na}^+ > \text{Mg}^{2+} \approx \text{K}^+ > \text{Ca}^{2+}$. As noted earlier, all salts are seen to interact and expand the monolayer. Evidence so far suggest Na^+ and Ca^{2+} bind more strongly to the phosphate headgroup than K^+ and Mg^{2+} , and while studies indicate some binding to the carbonyl moiety, binding to the phosphate is still the dominant mechanism. This is due to the location of phosphate group closer to the water region, and less sterically hindered than the carbonyl located deeper in the lipid region. In addition, the strong binding affinity of Na^+ and Ca^{2+} involve the dehydration of the phosphate group followed by formation of tight inner-sphere bonds. K^+ and Mg^{2+} on the other hand bind less strongly with the phosphate group and form solvent-separated pairs. This is attributed to the different matching water affinities and relative free energies.

However, binding strength alone cannot be used to explain the overall trend observed, as divalent and monovalent cations behave differently. While monovalent cations display primarily repulsive interactions both electrostatic and steric, divalent cations are capable of bridging lipid headgroups. The +2 charge can screen the negative

charges on the phosphate more efficiently than monovalent cations resulting in both reduced electrostatic and steric repulsion. This explains why although Na^+ and Ca^{2+} both bind to DPPA strongly, Na^+ expands the monolayer the most and Ca^{2+} the least.

The trends for Mg^{2+} and K^+ are much more complicated as they do not bind as strongly to DPPA. Although Mg^{2+} is a strong chaotrope and disrupts the hydrogen bonding of DPPA the most, as a divalent cation, it is also able to bridge neighboring DPPA molecules. While K^+ is a weak kosmotrope, and thus does not disrupt the hydrogen bond network as much, it also expands the monolayer due to steric repulsion. Thus the combination of varying competing forces: binding affinity, hydrogen bond disruption and steric volume, result in similar magnitudes of DPPA monolayer expansion, complicating direct comparisons between monovalent and divalent cations.

However, it is clear that DPPA on neat water is primarily dominated by hydrogen bonding, both intramolecular and water-mediated, and the absence of ions and steric hindrance due to its small headgroup size allow it to pack more tightly than any other subphase. The replacement of water by various cations serves to increase the mean molecular area occupied by each lipid molecule, and thus causes an expansion effect.

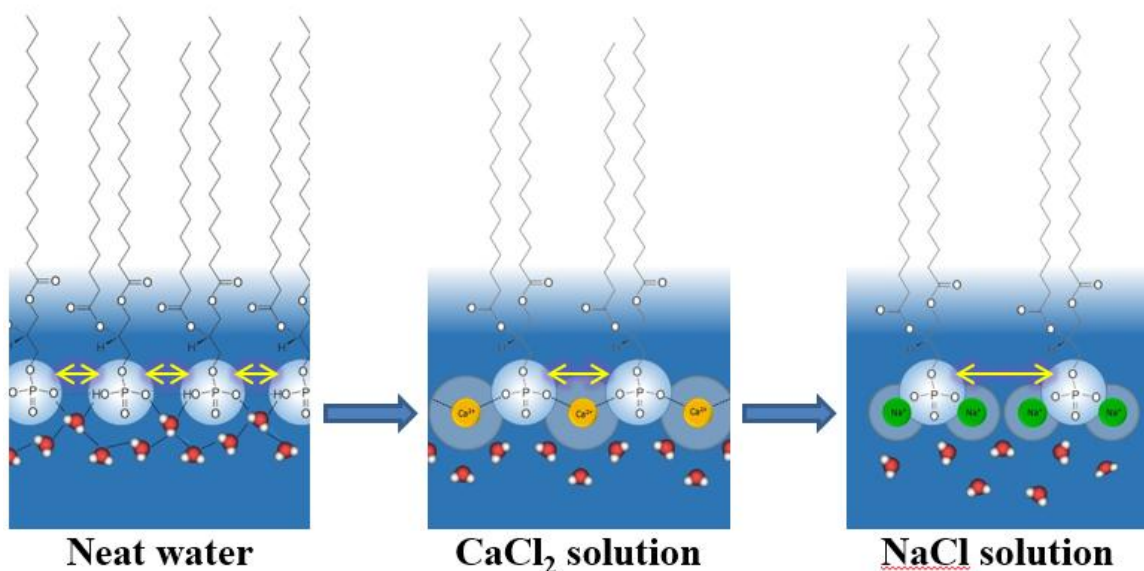


Figure 6 Visual representation of DPPA monolayer expansion on neat water, Ca^{2+} , and Na^+ solutions.

4.1.9 Phase behavior and surface propensity of LPS

Figure 4.22 shows the Π -A isotherm of LPS purified by phenol extraction on neat water and various NaCl subphases. LPS was found to be soluble only in water and no change in surface pressure upon compression is observed. This is characteristic of a Gibbs monolayer, where the surfactant forms a soluble monolayer as opposed to the insoluble DPPA monolayer. Thus compression of the monolayer simply drives LPS into the bulk. Upon the addition of increasing Na^+ concentrations to the subphase, an increase in surface pressure is observed. Na^+ increases the surface propensity of LPS, however the mechanism is not well understood. In addition, the CMC value of LPS has been reported to be $22 \mu\text{g/mL}$.⁶⁷ This low CMC value indicates LPS is likely to form 3-D structures such as aggregates and micelles.

LPS is extracted and purified by a variety of methods, such as phenol extraction mentioned above, and TCA extraction. Figure 4.21 shows the Π -A isotherm of LPS

purified by TCA extraction on neat water and various NaCl subphases. Although the trend is the same as that observed in phenol purified LPS, isotherms of TCA-purified LPS report in higher surface pressures. The difference between TCA and phenol purification is the presence of leftover proteins and RNA. TCA purification leaves up to 2% RNA and 10% protein while phenol purification leaves up to 60% RNA and 1% protein. The higher surface pressures can be attributed to the presence of proteins which may be surface active and interact with LPS.

Figure 4.24 shows the surface pressure of LPS without compression as a function of time. Upon spreading, a decrease in surface pressure is observed which drops sharply for ~45 min where upon it decreases stabilizes at a steady rate by the 2 h mark. This monolayer relaxation behavior has been observed in surfactant polymers, and a viscoelastic fit for shear relaxation can be made of the LPS relaxation isotherm. This indicates that LPS displays a degree of polymer-like behavior.

4.2 BAM Images

4.2.1 Monolayer morphology of DPPA

Figure 4.25 shows the BAM images of DPPA on neat water. Dark areas correspond to water- rich (lipid-poor) regions, while bright areas correspond to lipid-rich regions. At a surface pressure of 0 mN/m, the morphology of DPPA shows large island domains. This supports compression isotherms that show DPPA starting in the LE-LC phase and lacking a LE or G phase. The large island domains separated by areas of water indicate a LE-LC coexistence region where increased interactions between the monolayers exist in the LC phase, but are also fluid-like and separated by some distances

in the LE phase. Upon liftoff, the islands close up and DPPA adopts a homogenous closely packed morphology indicating transition into a purely LC phase. Further compression does not change the morphology, even in the collapse phase. DPPA stays relatively homogeneous, forming bilayers or trilayers instead of aggregating into smaller structures due to intramolecular hydrogen bonding. Although other lipid monolayers such as DPPG and DPPE are capable of hydrogen bonding interactions, they do not display the continuous homogenous film morphology characteristic of DPPA. This indicates that DPPA has an unusually high degree of hydrogen bonding compared to other phospholipids.

Figures 4.26, 4.27, and 4.28 show the BAM images of DPPA on the various salt solutions. There are few discernible differences, except in the collapse phase where elongated white 3-D structures appear. These have been reported before by Minones et al.; unfortunately, the understanding of 3-D collapse structure is still limited.⁸² One exception is the collapse morphology of DPPA with K^+ . No structures are observed, indicating a squeeze out of K^+ at a high compression area, and a weak binding of K^+ to DPPA as discussed previously. The overall trend reveals that Na^+ , K^+ , Mg^{2+} , and Ca^{2+} have little impact on the morphology of DPPA. This has implications for organic aerosols, which suggest the morphology of insoluble DPPA films coating an aerosol surface are insensitive to the composition of aerosols and maintain their homogeneous nature.

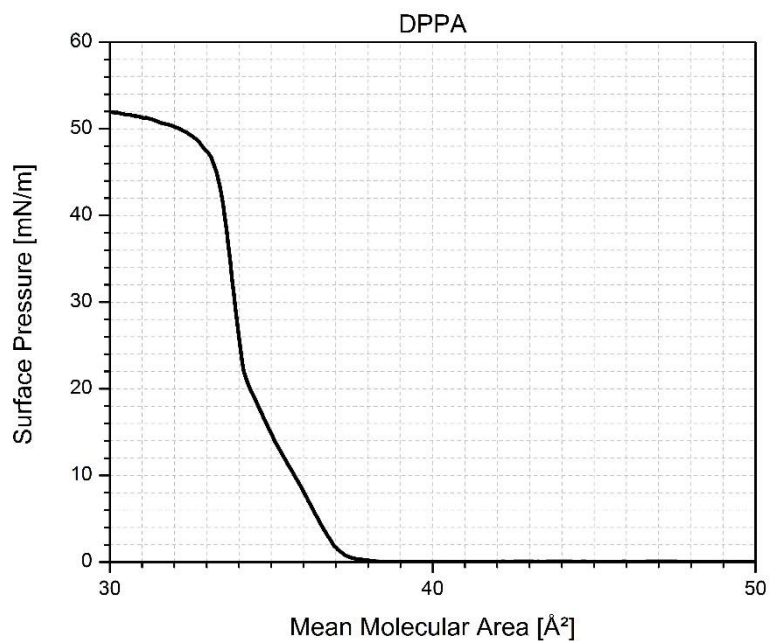


Figure 4.7 Π -A isotherm of DPPA monolayer on nanopure water.

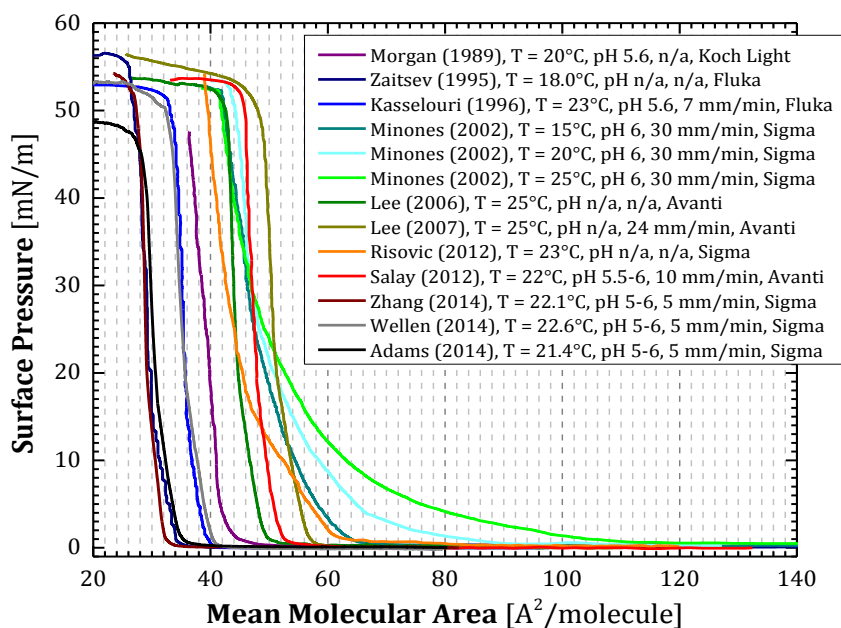


Figure 4.8 Literature Π -A isotherms of DPPA monolayers on water (courtesy of Dr. Dominique Verreault).

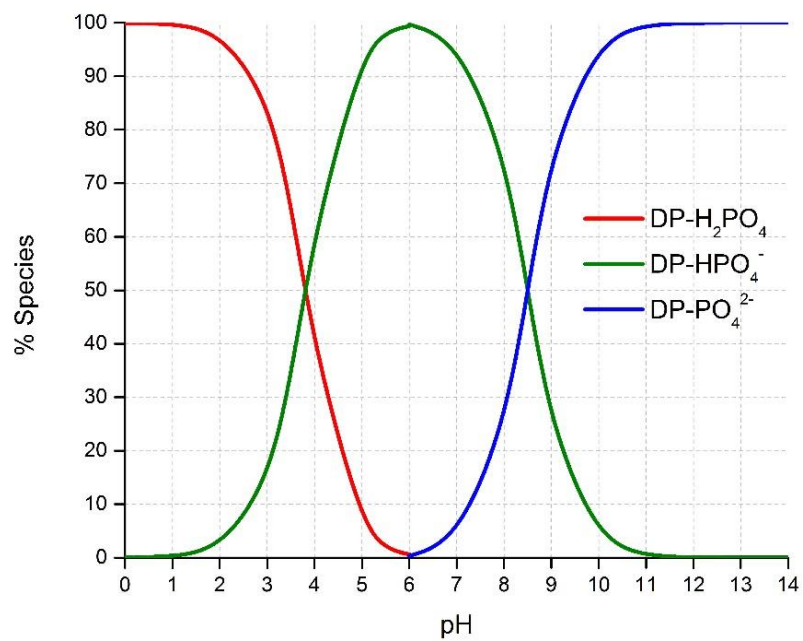


Figure 4.9 Speciation curves of DPPA in water.

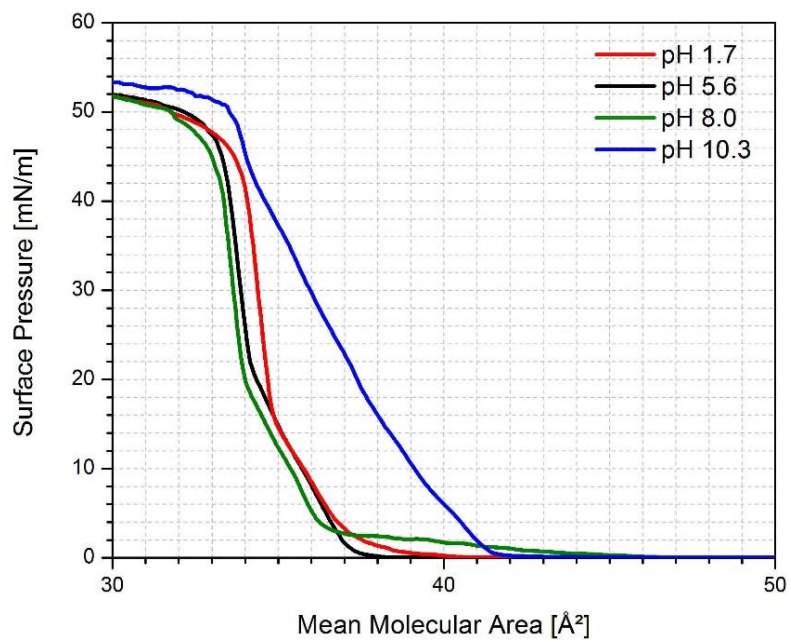


Figure 4.10 Π -A isotherms of DPPA monolayers on nanopure water at various pH.

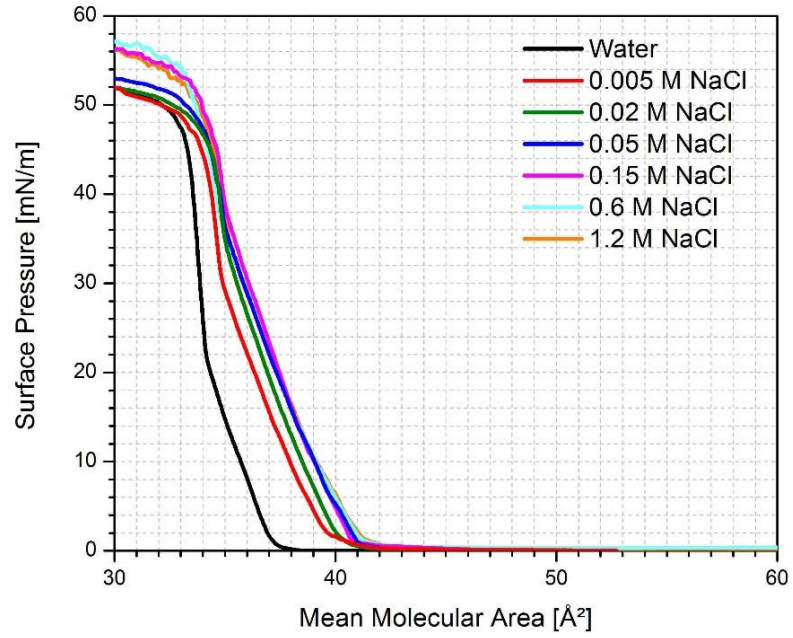


Figure 4.11 Π -A isotherms of DPPA monolayers on NaCl solutions.

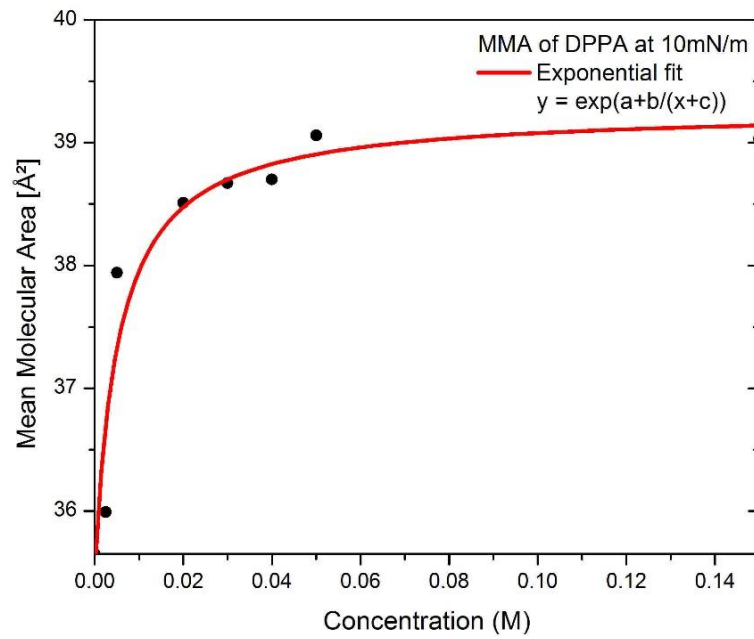


Figure 4.12 Saturation curve of DPPA monolayers on NaCl solutions.

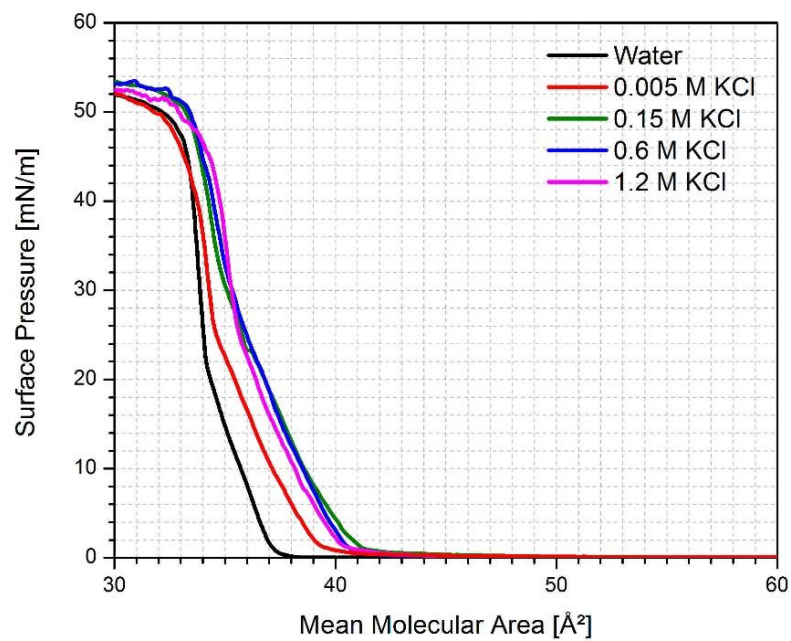


Figure 4.13 Π -A isotherms of DPPA monolayers on KCl solutions.

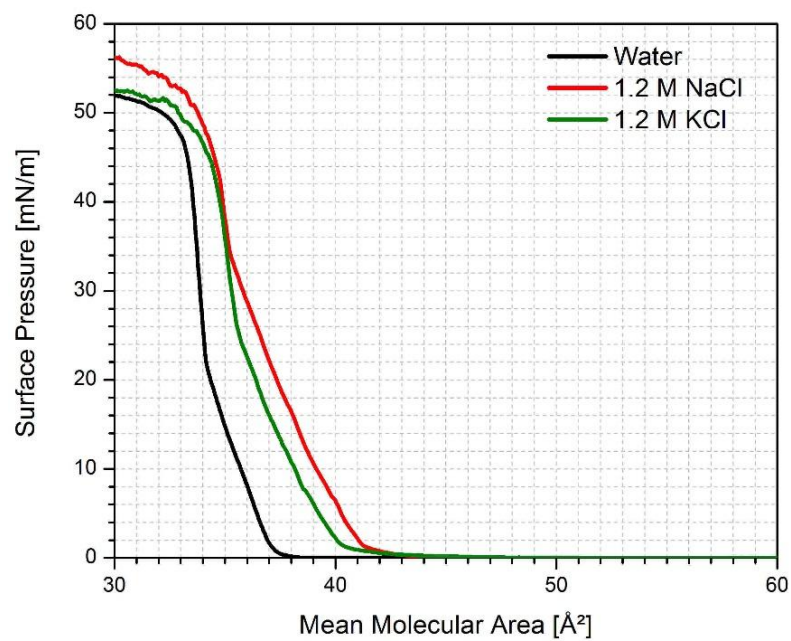


Figure 4.14 Π -A isotherms of DPPA monolayers on monovalent chloride salts.

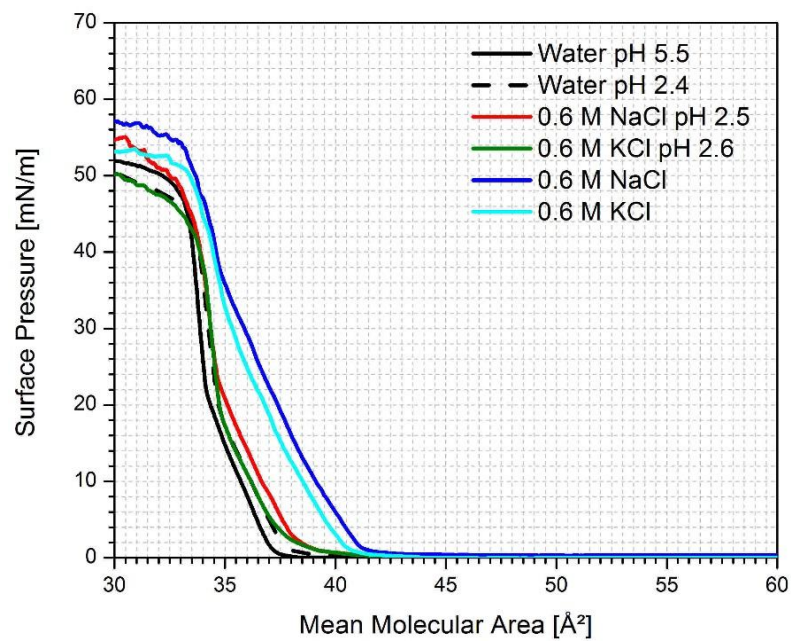


Figure 4.15 Π -A isotherms of DPPA monolayers on monovalent chloride salts at acidic pH.

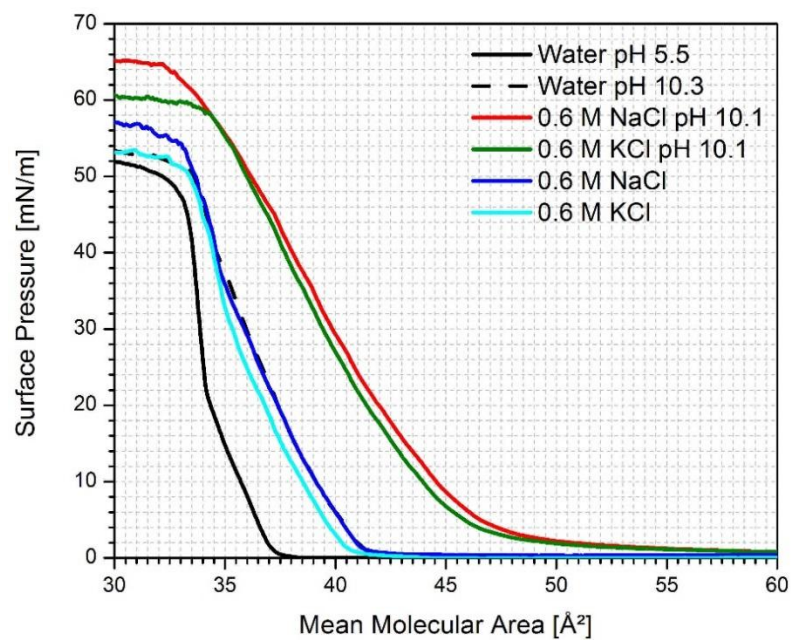


Figure 4.16 Π -A isotherms of DPPA monolayers on monovalent chloride salts at basic pH.

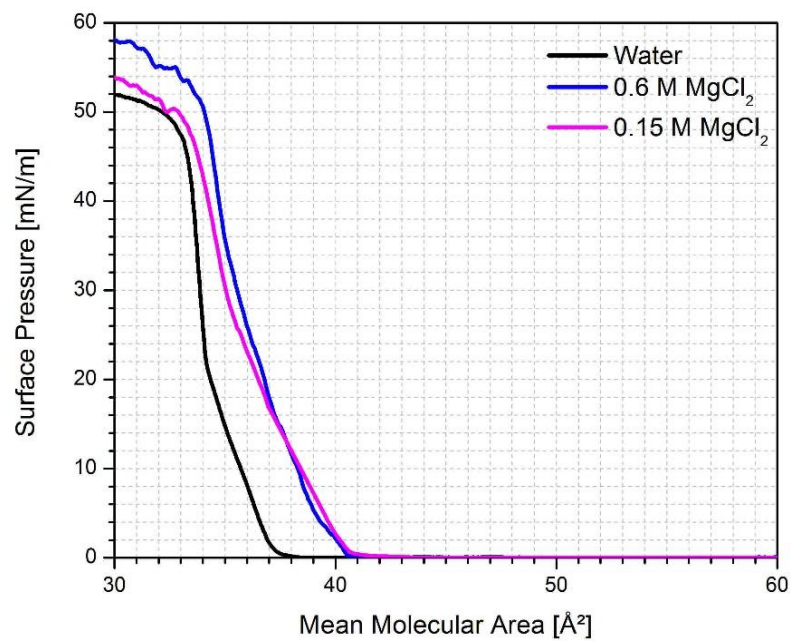


Figure 4.17 Π -A isotherms of DPPA monolayers on MgCl_2 solutions.

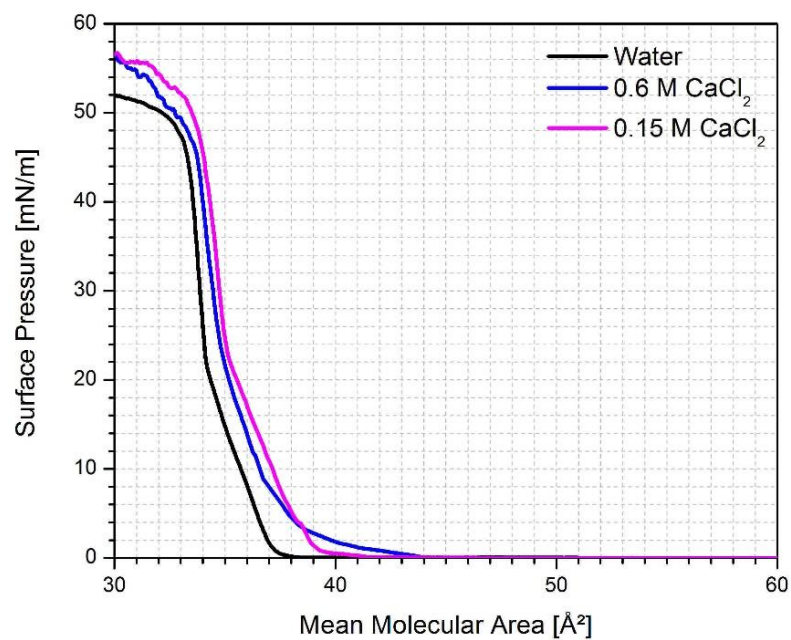


Figure 4.18 Π -A isotherms of DPPA monolayers on CaCl_2 solutions.

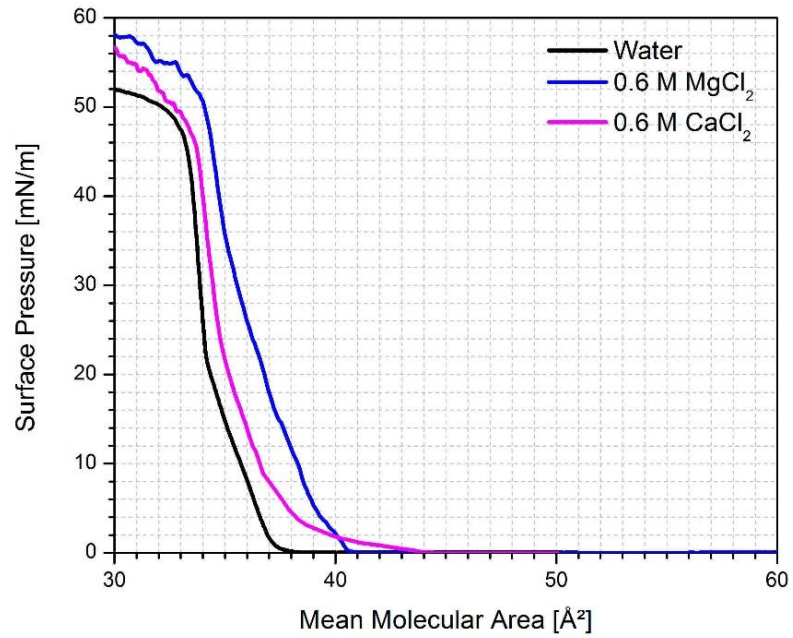


Figure 4.19 Π -A isotherm of DPPA monolayer on divalent salts.

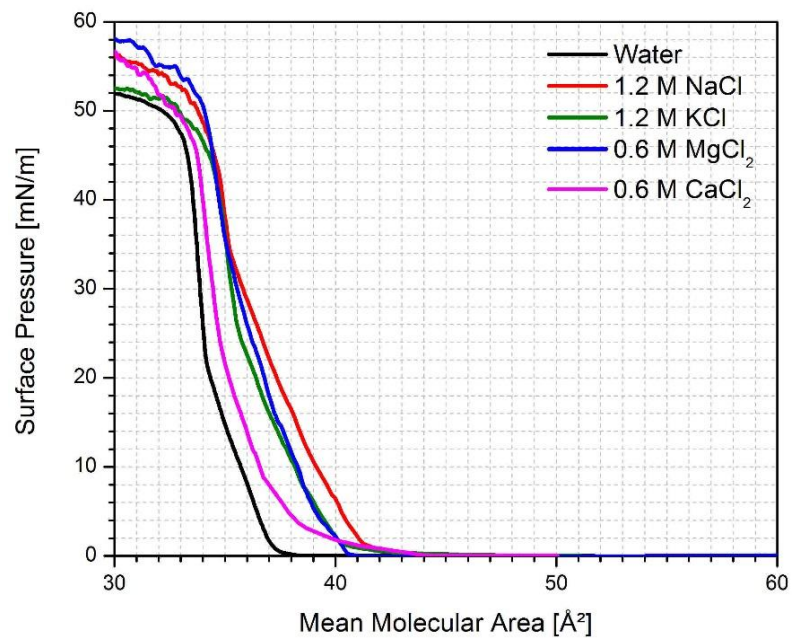


Figure 4.20 Π -A isotherms of DPPA monolayers on all chloride salts.

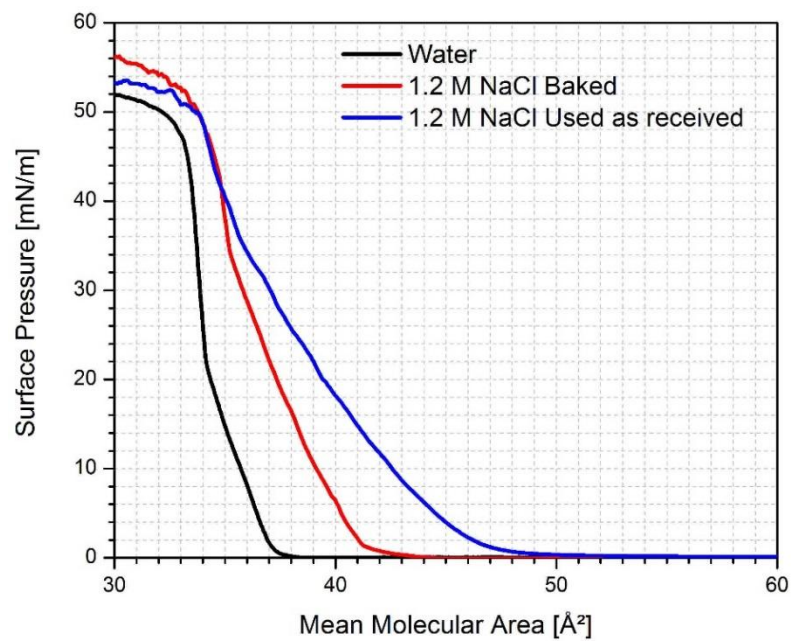


Figure 4.21 Π -A isotherms of DPPA monolayers on NaCl, baked and used as received.

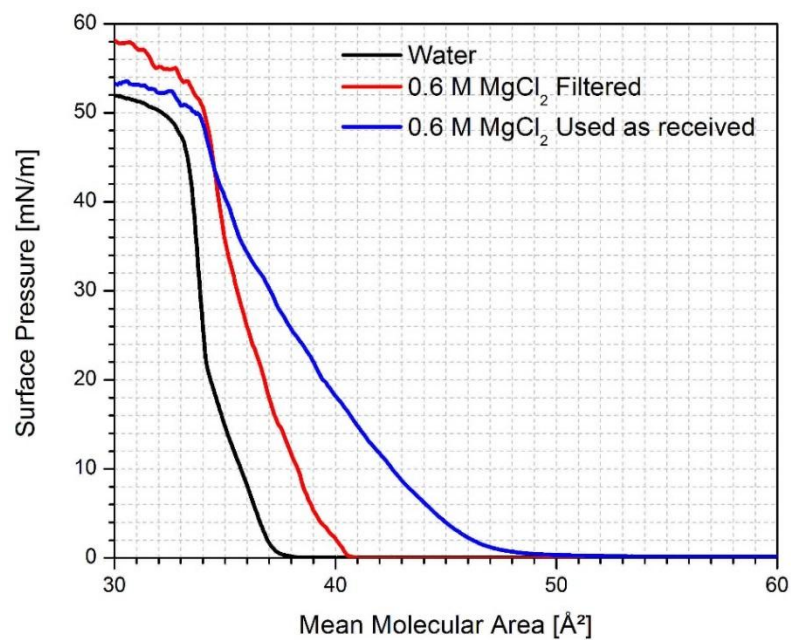


Figure 4.22 Π -A isotherms of DPPA monolayers on $MgCl_2$, baked and used as received.

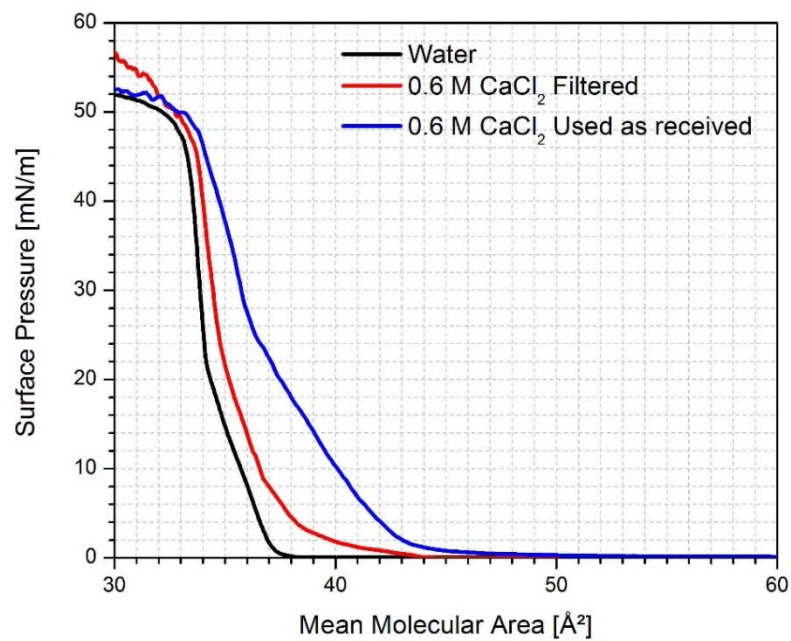


Figure 4.23 Π -A isotherms of DPPA monolayers on CaCl_2 , baked and used as received.

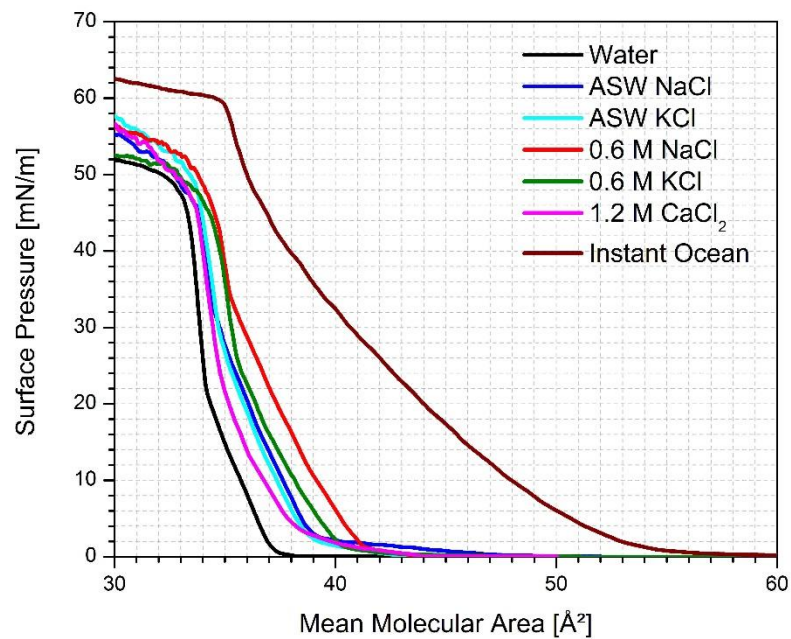


Figure 4.24 Π -A isotherms of DPPA monolayers on chloride salts, and custom-made and commercial ASW.

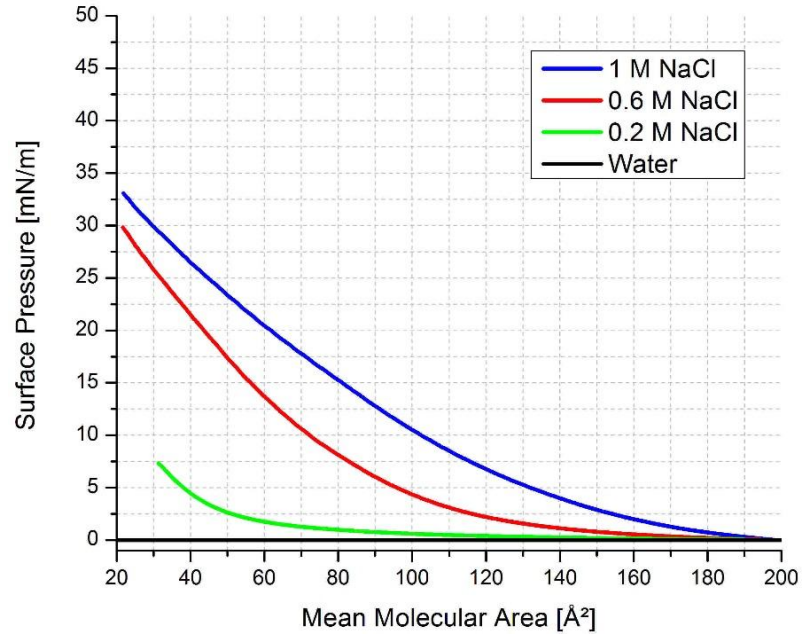


Figure 4.25 Π -A isotherm of phenol-purified LPS.

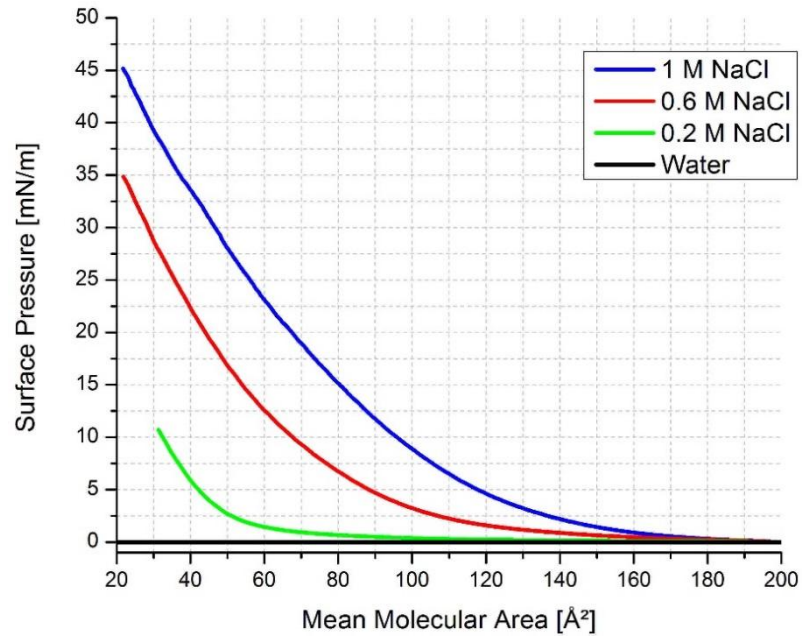


Figure 4.26 Π -A isotherm of TCA-purified LPS.

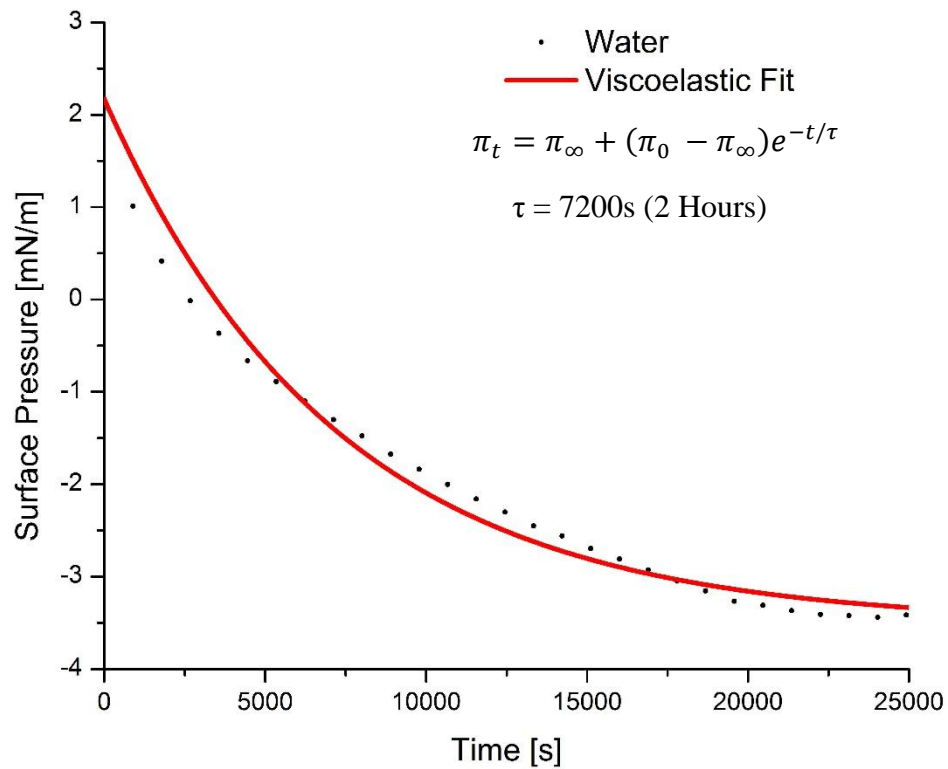


Figure 4.27 Relaxation curve of LPS. Experimental data (solid line) and viscoelastic fit (dashed line) are shown.

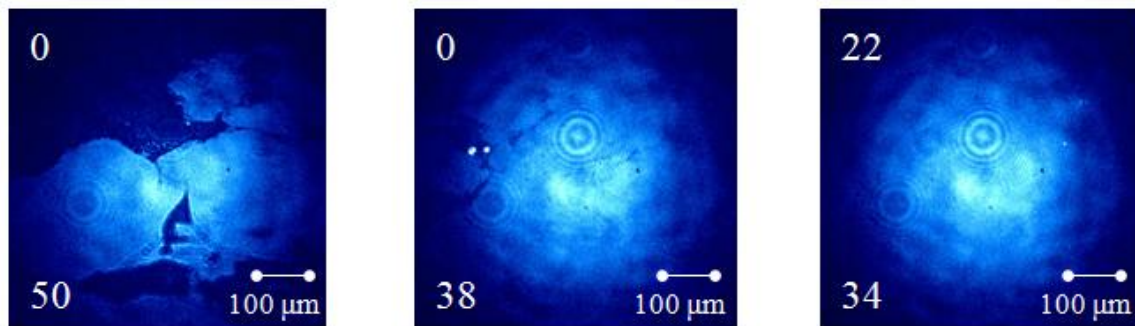


Figure 28 BAM images of a DPPA monolayer on water during compression. Numbers in the lower and upper left corners indicate the mean molecular area and the surface pressure, respectively.

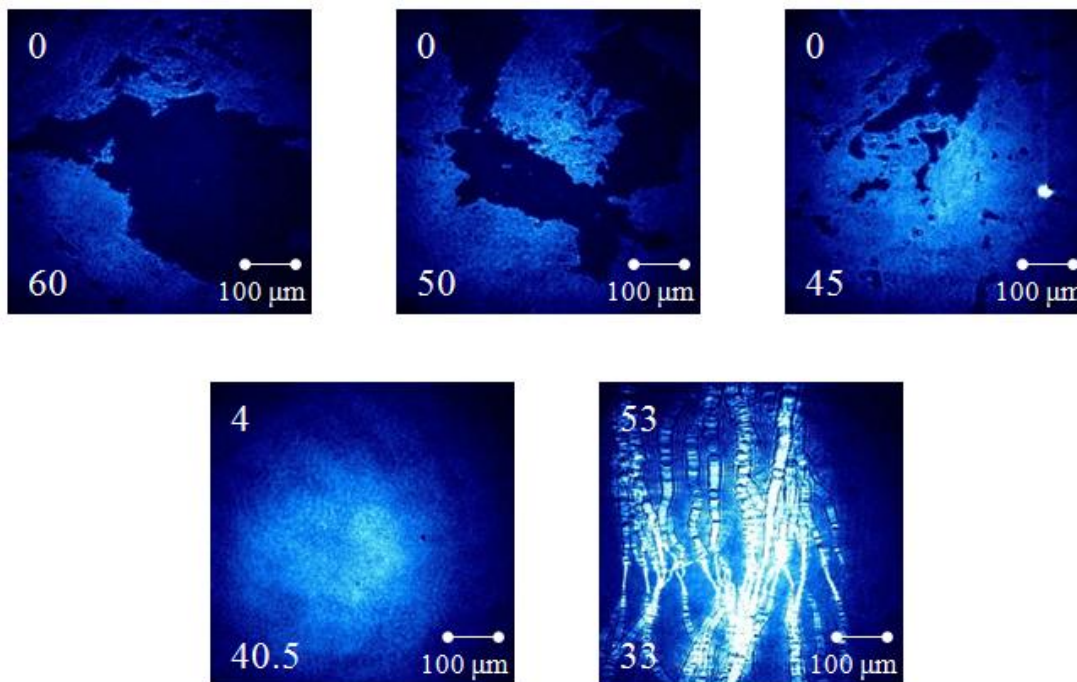


Figure 29 BAM images of DPPA monolayer on NaCl solution during compression. Numbers in the lower and upper left corners indicate the mean molecular area and the surface pressure, respectively.

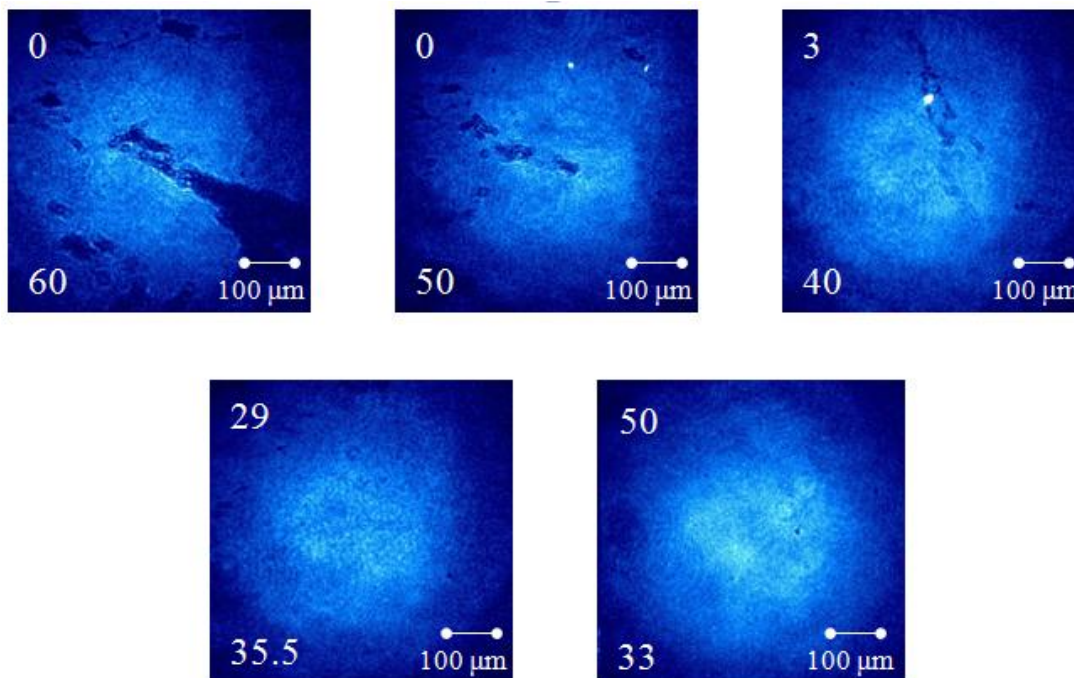


Figure 30 BAM images of DPPA monolayer on KCl solution during compression. Numbers in the lower and upper left corners indicate the mean molecular area and the surface pressure, respectively.

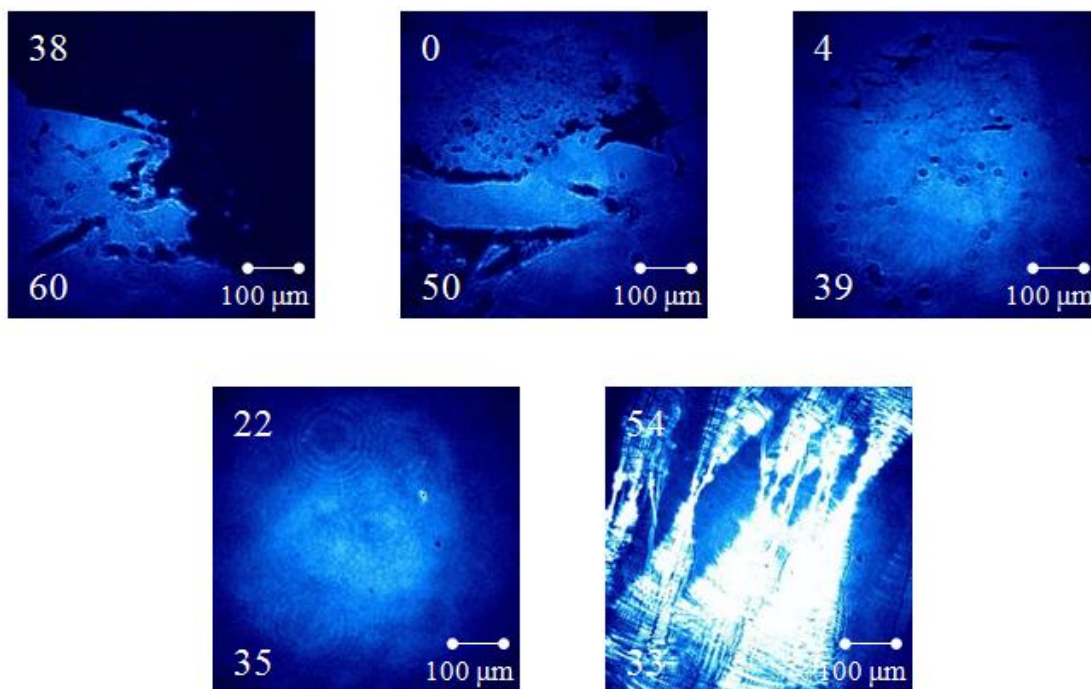


Figure 31 BAM images of DPPA monolayer on MgCl_2 solution during compression. Numbers in the lower and upper left corners indicate the mean molecular area and the surface pressure, respectively.

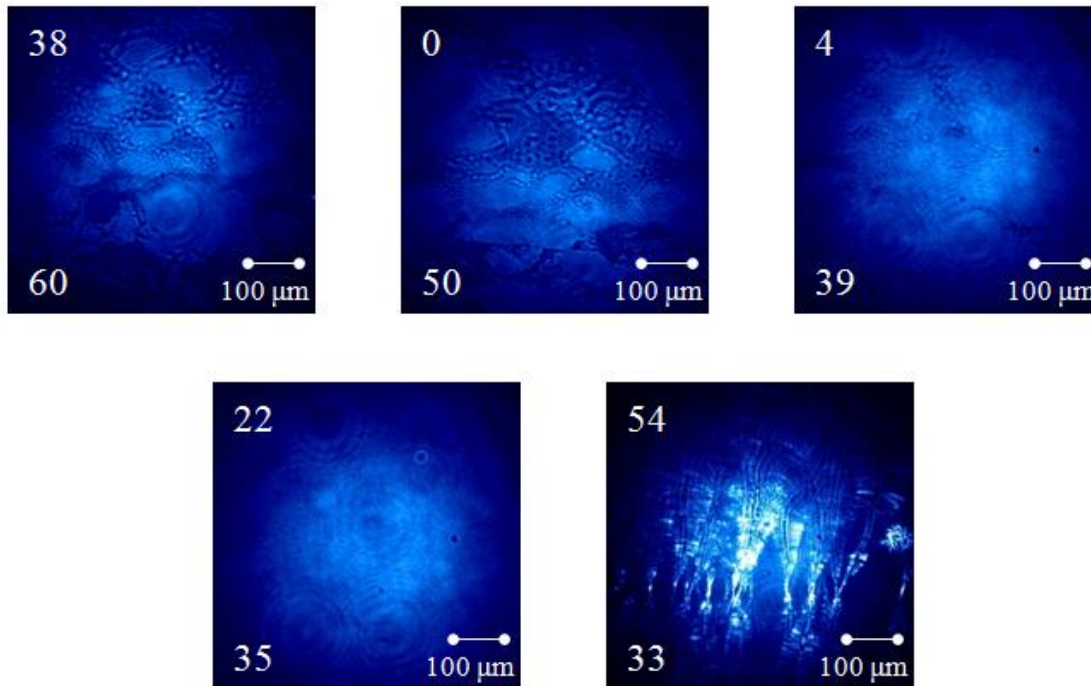


Figure 32 BAM images of DPPA monolayer on CaCl_2 solution during compression. Numbers in the lower and upper left corners indicate the mean molecular area and the surface pressure, respectively.

Chapter 5: Conclusions and Future Work

In this thesis, the surface tension of LPS and DPPA on neat water and various salt solutions was studied by means of surface pressure-area isotherms. In addition, surface morphology of DPPA was investigated with BAM.

DPPA on neat water displayed phase behavior that indicated a tight degree of packing. Presence of cations reduced the degree of packing, due to a net repulsive effect between competing hydrogen bonding, sterics, and electrostatic interactions. DPPA displays a much larger degree of hydrogen bonding than other phospholipids due to its unique small headgroup size. This in turn is responsible for DPPA's low area occupied per lipid molecule as well as its unique surface morphology seen in the BAM studies

DPPA forms a homogenous continuous monolayer that is morphologically insensitive to the addition of Na^+ , K^+ , Mg^{2+} , or Ca^{2+} . DPPA forms large island domains that quickly combine due to the extensive hydrogen bonding. The presence of a smooth continuous film with no open areas of water on the surface of aerosols has critical implications for aerosol properties, such as water evaporation rate and ability to serve as ice nucleation sites.

Differences between monovalent ions and their relative binding affinities were observed based on their relative expansion of the DPPA monolayer, with Na^+ having a greater binding affinity for DPPA than K^+ . Ca^{2+} has a greater binding affinity than Mg^{2+} which results in less expanded monolayers due to the unique properties of divalent

cations. Due to the different mechanisms involved in monovalent and divalent cation binding, such as the bridging effects, a direct comparison between the two groups cannot be made. The cation specificity of DPPA molecules is reflected in its important biological cell functions, for maintaining cell membranes with different ion concentrations in the cytosol and blood. There may also be additional effects in marine aerosols with different salt compositions. The importance of Mg^{2+} in biological systems found in the sea surface microlayer has been a hotly studied topic. Phospholipids and other surfactants of biological origin that are incorporated into marine aerosols, and their interaction with Mg^{2+} as well as Ca^{2+} , which are common ocean cations, are still not fully understood.

LPS was observed to form soluble monolayers on water, due to the nature of many sugar groups in the structure. LPS surface propensity was found to increase with the addition of Na^+ , which is the most abundant ocean cation, suggesting the presence of LPS on the surface of marine aerosols. A constant decrease in surface pressure was observed, attributed to relaxation of the monolayer. This suggests LPS displays surface behavior similar to that of proteins and polymers.

Future work for this work involves further experiments to distinguish the differences in DPPA interaction between Ca^{2+} and Mg^{2+} . Experiments of these cations with different ionization states of DPPA at acidic and basic pH will shed light on the nature of comparative binding affinity of Ca^{2+} and Mg^{2+} . Such studies would be aided by detailed DPPA saturation studies of K^+ , Ca^{2+} , and Mg^{2+} , as well which are lacking in this study. Surface specific spectroscopic studies such as infrared reflection absorption spectroscopy will can provide more detailed chemical information such as the alkyl chain orientation and tilt angle of DPPA to reveal the structure of the packed monolayer.

Further BAM studies on the morphology of DPPA monolayers are also needed particularly at acidic and basic conditions for neat water and all subphases. In the particular, the highly expanded nature of DPPA monolayers at pH 10 may display a different morphology from that of the continuous homogenous film seen. Also of interest are the monolayer properties of DPPA at different temperatures. As the phase behavior of lipids is dependent on their phase transition temperature, the monolayer behavior of DPPA may differ at temperatures different from room temperature.

As marine aerosols are not single surfactant systems, but contain many different molecules, studies of mixed monolayers of DPPA and LPS as a more complex model system are expected. DPPA is a proxy for phospholipids and LPS for bacteria, and surface pressure-area isotherms of these mixtures will give more detailed chemical knowledge of interactions and reactions of various surfactants on the surface of marine aerosols.

References

1. Stocker, T., *Climate change 2013 : the physical science basis : Working Group I contribution to the Fifth assessment report of the Intergovernmental Panel on Climate Change*. Cambridge University Press: New York, 2014; p xi, 1535 pages.
2. Murphy, D. M.; Thomson, D. S.; Mahoney, T. M. J., In situ measurements of organics, meteoritic material, mercury, and other elements in aerosols at 5 to 19 kilometers. *Science* **1998**, *282* (5394), 1664-1669.
3. Lohmann, U.; Feichter, J., Global indirect aerosol effects: a review. *Atmos Chem Phys* **2005**, *5*, 715-737.
4. Lihavainen, H.; Kerminen, V. M.; Komppula, M.; Hyvarinen, A. P.; Laakia, J.; Saarikoski, S.; Makkonen, U.; Kivekas, N.; Hillamo, R.; Kulmala, M.; Viisanen, Y., Measurements of the relation between aerosol properties and microphysics and chemistry of low level liquid water clouds in Northern Finland. *Atmos Chem Phys* **2008**, *8* (23), 6925-6938.
5. Twomey, S., Pollution and Planetary Albedo. *Atmos Environ* **1974**, *8* (12), 1251-1256.
6. Penner, J. E.; Quaas, J.; Storelvmo, T.; Takemura, T.; Boucher, O.; Guo, H.; Kirkevag, A.; Kristjansson, J. E.; Seland, O., Model intercomparison of indirect aerosol effects. *Atmos Chem Phys* **2006**, *6*, 3391-3405.
7. Koren, I.; Remer, L. A.; Kaufman, Y. J.; Rudich, Y.; Martins, J. V., On the twilight zone between clouds and aerosols. *Geophys Res Lett* **2007**, *34* (8).
8. Goosse, H.; Barriat, P. Y.; Lefebvre, W.; Loutre, M. F.; Zunz, V., Introduction to climate dynamics and climate modeling. 2014. <http://www.climate.be/textbook>.
9. Gill, P. S.; Graedel, T. E.; Weschler, C. J., Organic Films on Atmospheric Aerosol-Particles, Fog Droplets, Cloud Droplets, Raindrops, and Snowflakes. *Rev Geophys* **1983**, *21* (4), 903-920.
10. Ellison, G. B.; Tuck, A. F.; Vaida, V., Atmospheric processing of organic aerosols. *J Geophys Res-Atmos* **1999**, *104* (D9), 11633-11641.
11. Andrews, E.; Larson, S. M., Effect of Surfactant Layers on the Size Changes of Aerosol-Particles as a Function of Relative-Humidity. *Environ Sci Technol* **1993**, *27* (5), 857-865.
12. Finlayson-Pitts, B. J.; Pitts, J. N., *Chemistry of the upper and lower atmosphere : theory, experiments, and applications*. Academic Press: San Diego, 2000; p xxii, 969 p.
13. Clifford, D.; Bartels-Rausch, T.; Donaldson, D. J., Suppression of aqueous surface hydrolysis by monolayers of short chain organic amphiphiles. *Phys Chem Chem Phys* **2007**, *9* (11), 1362-1369.
14. Glass, S. V.; Park, S. C.; Nathanson, G. M., Evaporation of water and uptake of HCl and HBr through hexanol films at the surface of supercooled sulfuric acid. *J Phys Chem A* **2006**, *110* (24), 7593-7601.
15. Moroi, Y.; Rusdi, M.; Kubo, I., Difference in surface properties between insoluble monolayer and adsorbed film from kinetics of water evaporation and BAM image. *J Phys Chem B* **2004**, *108* (20), 6351-6358.
16. Beaver, M. R.; Freedman, M. A.; Hasenkopf, C. A.; Tolbert, M. A., Cooling Enhancement of Aerosol Particles Due to Surfactant Precipitation. *J Phys Chem A* **2010**, *114* (26), 7070-7076.

17. Reeser, D. I.; Kwamena, N. O. A.; Donaldson, D. J., Effect of Organic Coatings on Gas-Phase Nitrogen Dioxide Production from Aqueous Nitrate Photolysis. *J Phys Chem C* **2013**, *117* (43), 22260-22267.
18. Rinaldi, M.; Decesari, S.; Finessi, E.; Giulianelli, L.; Carbone, C.; Fuzzi, S.; O'Dowd, C. D.; Ceburnis, D.; Facchini, M. C., Primary and Secondary Organic Marine Aerosol and Oceanic Biological Activity: Recent Results and New Perspectives for Future Studies. *Adv Meteorol* **2010**.
19. Barger, W. R.; Garrett, W. D., Surface Active Organic Material in Marine Atmosphere. *J Geophys Res* **1970**, *75* (24), 4561-&.
20. Barger, W. R.; Garrett, W. D., Surface-Active Organic Material in Air over Mediterranean and over Eastern Equatorial Pacific. *J Geophys Res-Oc Atm* **1976**, *81* (18), 3151-3157.
21. Soloviev, A.; Lukas, R., *The near-surface layer of the ocean : structure, dynamics and applications*. Springer: Dordrecht, 2006; p xiv, 572 p.
22. Cunliffe, M.; Upstill-Goddard, R. C.; Murrell, J. C., Microbiology of aquatic surface microlayers. *Fems Microbiol Rev* **2011**, *35* (2), 233-246.
23. Cunliffe, M.; Engel, A.; Frka, S.; Gasparovic, B.; Guitart, C.; Murrell, J. C.; Salter, M.; Stolle, C.; Upstill-Goddard, R.; Wurl, O., Sea surface microlayers: A unified physicochemical and biological perspective of the air-ocean interface. *Prog Oceanogr* **2013**, *109*, 104-116.
24. Cunliffe, M.; Murrell, J. C., The sea-surface microlayer is a gelatinous biofilm. *Isme J* **2009**, *3* (9), 1001-1003.
25. O'Dowd, C. D.; Facchini, M. C.; Cavalli, F.; Ceburnis, D.; Mircea, M.; Decesari, S.; Fuzzi, S.; Yoon, Y. J.; Putaud, J. P., Biogenically driven organic contribution to marine aerosol. *Nature* **2004**, *431* (7009), 676-680.
26. Yoon, Y. J.; Ceburnis, D.; Cavalli, F.; Jourdan, O.; Putaud, J. P.; Facchini, M. C.; Decesari, S.; Fuzzi, S.; Sellegri, K.; Jennings, S. G.; O'Dowd, C. D., Seasonal characteristics of the physicochemical properties of North Atlantic marine atmospheric aerosols. *J Geophys Res-Atmos* **2007**, *112* (D4).
27. O'Dowd, C. D.; De Leeuw, G., Marine aerosol production: a review of the current knowledge. *Philos T R Soc A* **2007**, *365* (1856), 1753-1774.
28. Wallace, G. T.; Duce, R. A., Transport of Particulate Organic-Matter by Bubbles in Marine Waters. *Limnol Oceanogr* **1978**, *23* (6), 1155-1167.
29. Millero, F. J.; Feistel, R.; Wright, D. G.; McDougall, T. J., The composition of Standard Seawater and the definition of the Reference-Composition Salinity Scale. *Deep-Sea Res Pt I* **2008**, *55* (1), 50-72.
30. Ault, A. P.; Moffet, R. C.; Baltrusaitis, J.; Collins, D. B.; Ruppel, M. J.; Cuadra-Rodriguez, L. A.; Zhao, D. F.; Guasco, T. L.; Ebben, C. J.; Geiger, F. M.; Bertram, T. H.; Prather, K. A.; Grassian, V. H., Size-Dependent Changes in Sea Spray Aerosol Composition and Properties with Different Seawater Conditions. *Environ Sci Technol* **2013**, *47* (11), 5603-5612.
31. Tang, C. Y.; Huang, Z. S. A.; Allen, H. C., Binding of Mg²⁺ and Ca²⁺ to Palmitic Acid and Deprotonation of the COOH Headgroup Studied by Vibrational Sum Frequency Generation Spectroscopy. *J Phys Chem B* **2010**, *114* (51), 17068-17076.
32. Tang, C. Y.; Huang, Z. S.; Allen, H. C., Interfacial Water Structure and Effects of Mg²⁺ and Ca²⁺ Binding to the COOH Headgroup of a Palmitic Acid Monolayer Studied by Sum Frequency Spectroscopy. *J Phys Chem B* **2011**, *115* (1), 34-40.
33. Tang, C. Y.; Allen, H. C., Ionic Binding of Na⁺ versus K⁺ to the Carboxylic Acid Headgroup of Palmitic Acid Monolayers Studied by Vibrational Sum Frequency Generation Spectroscopy. *J Phys Chem A* **2009**, *113* (26), 7383-7393.

34. Lee, Y. L.; Lin, J. Y.; Lee, S., Adsorption behavior of glucose oxidase on a dipalmitoylphosphatic acid monolayer and the characteristics of the mixed monolayer at air/liquid interfaces. *Langmuir* **2007**, *23* (4), 2042-2051.
35. Tervahattu, H.; Juhanoja, J.; Kupiainen, K., Identification of an organic coating on marine aerosol particles by TOF-SIMS. *J Geophys Res-Atmos* **2002**, *107* (D16).
36. Marty, J. C.; Saliot, A.; Buatmenard, P.; Chesselet, R.; Hunter, K. A., Relationship between the Lipid Compositions of Marine Aerosols, the Sea-Surface Microlayer, and Subsurface Water. *J Geophys Res-Oc Atm* **1979**, *84* (Nc9), 5707-5716.
37. Brandsma, J.; Hopmans, E. C.; Brussaard, C. P. D.; Witte, H. J.; Schouten, S.; Damste, J. S. S., Spatial distribution of intact polar lipids in North Sea surface waters: Relationship with environmental conditions and microbial community composition. *Limnol Oceanogr* **2012**, *57* (4), 959-973.
38. Close, H. G.; Wakeham, S. G.; Pearson, A., Lipid and C-13 signatures of submicron and suspended particulate organic matter in the Eastern Tropical North Pacific: Implications for the contribution of Bacteria. *Deep-Sea Res Pt I* **2014**, *85*, 15-34.
39. Espinosa, L. F.; Pantoja, S.; Pinto, L. A.; Rullkotter, J., Water column distribution of phospholipid-derived fatty acids of marine microorganisms in the Humboldt Current system off northern Chile. *Deep-Sea Res Pt II* **2009**, *56* (16), 1039-1048.
40. Hakvag, S.; Fjaervik, E.; Josefsen, K. D.; Ian, E.; Ellingsen, T. E.; Zotchev, S. B., Characterization of Streptomyces spp. Isolated from the Sea Surface Microlayer in the Trondheim Fjord, Norway. *Mar Drugs* **2008**, *6* (4), 620-635.
41. Hakvag, S.; Fjaervik, E.; Klinkenberg, G.; Borgos, S. E. F.; Josefsen, K. D.; Ellingsen, T. E.; Zotchev, S. B., Violacein-Producing Collimonas sp from the Sea Surface Microlayer of Coastal Waters in Trondelag, Norway. *Mar Drugs* **2009**, *7* (4), 576-588.
42. Canadas, O.; Garcia-Verdugo, I.; Keough, K. M. W.; Casals, C., SP-A permeabilizes lipopolysaccharide membranes by forming protein aggregates that extract lipids from the membrane. *Biophys J* **2008**, *95* (7), 3287-3294.
43. Garcia-Verdugo, I.; Canadas, O.; Taneva, S. G.; Keough, K. M. W.; Casals, C., Surfactant protein a forms extensive lattice-like structures on 1,2-dipalmitoylphosphatidylcholine/rough-Lipopolysaccharide-Mixed monolayers. *Biophys J* **2007**, *93* (10), 3529-3540.
44. Yang, H. Y.; Roberts, M. F., Phosphohydrolase and transphosphatidyltransferase reactions of two Streptomyces phospholipase D enzymes: Covalent versus noncovalent catalysis. *Protein Sci* **2003**, *12* (9), 2087-2098.
45. Jimenez, J. L.; Canagaratna, M. R.; Donahue, N. M.; Prevot, A. S. H.; Zhang, Q.; Kroll, J. H.; DeCarlo, P. F.; Allan, J. D.; Coe, H.; Ng, N. L.; Aiken, A. C.; Docherty, K. S.; Ulbrich, I. M.; Grieshop, A. P.; Robinson, A. L.; Duplissy, J.; Smith, J. D.; Wilson, K. R.; Lanz, V. A.; Hueglin, C.; Sun, Y. L.; Tian, J.; Laaksonen, A.; Raatikainen, T.; Rautiainen, J.; Vaattovaara, P.; Ehn, M.; Kulmala, M.; Tomlinson, J. M.; Collins, D. R.; Cubison, M. J.; Dunlea, E. J.; Huffman, J. A.; Onasch, T. B.; Alfarra, M. R.; Williams, P. I.; Bower, K.; Kondo, Y.; Schneider, J.; Drewnick, F.; Borrmann, S.; Weimer, S.; Demerjian, K.; Salcedo, D.; Cottrell, L.; Griffin, R.; Takami, A.; Miyoshi, T.; Hatakeyama, S.; Shimojo, A.; Sun, J. Y.; Zhang, Y. M.; Dzepina, K.; Kimmel, J. R.; Sueper, D.; Jayne, J. T.; Herndon, S. C.; Trimborn, A. M.; Williams, L. R.; Wood, E. C.; Middlebrook, A. M.; Kolb, C. E.; Baltensperger, U.; Worsnop, D. R., Evolution of Organic Aerosols in the Atmosphere. *Science* **2009**, *326* (5959), 1525-1529.
46. Kroll, J. H.; Seinfeld, J. H., Chemistry of secondary organic aerosol: Formation and evolution of low-volatility organics in the atmosphere. *Atmos Environ* **2008**, *42* (16), 3593-3624.
47. Hallquist, M.; Wenger, J. C.; Baltensperger, U.; Rudich, Y.; Simpson, D.; Claeys, M.; Dommen, J.; Donahue, N. M.; George, C.; Goldstein, A. H.; Hamilton, J. F.; Herrmann, H.;

- Hoffmann, T.; Iinuma, Y.; Jang, M.; Jenkin, M. E.; Jimenez, J. L.; Kiendler-Scharr, A.; Maenhaut, W.; McFiggans, G.; Mentel, T. F.; Monod, A.; Prevot, A. S. H.; Seinfeld, J. H.; Surratt, J. D.; Szmigielski, R.; Wildt, J., The formation, properties and impact of secondary organic aerosol: current and emerging issues. *Atmos Chem Phys* **2009**, *9* (14), 5155-5236.
48. Goddard, E. D.; Ananthapadmanabhan, K. P., *Interactions of surfactants with polymers and proteins*. CRC Press: Boca Raton, 1993; p 427 p.
49. Kooijman, E. E.; Testerink, C., Phosphatidic Acid: An Electrostatic/Hydrogen-Bond Switch? *Plant Cell Monogr* **2010**, *16*, 203-222.
50. Eaton, J. M.; Takkellapati, S.; Lawrence, R. T.; McQueeney, K. E.; Boroda, S.; Mullins, G. R.; Sherwood, S. G.; Finck, B. N.; Villen, J.; Harris, T. E., Lipin 2 Binds Phosphatidic Acid by the Electrostatic Hydrogen Bond Switch Mechanism Independent of Phosphorylation. *J Biol Chem* **2014**, *289* (26), 18055-18066.
51. Kooijman, E. E.; Chupin, V.; de Kruijff, B.; Burger, K. N. J., Modulation of membrane curvature by phosphatidic acid and lysophosphatidic acid. *Traffic* **2003**, *4* (3), 162-174.
52. Mengistu, D. H.; Kooijman, E. E.; May, S., Ionization properties of mixed lipid membranes: A Gouy-Chapman model of the electrostatic-hydrogen bond switch. *Bba-Biomembranes* **2011**, *1808* (8), 1985-1992.
53. Kooijman, E. E.; Tieleman, D. P.; Testerink, C.; Munnik, T.; Rijkers, D. T. S.; Burger, K. N. J.; de Kruijff, B., An electrostatic/hydrogen bond switch as the basis for the specific interaction of phosphatidic acid with proteins. *J Biol Chem* **2007**, *282* (15), 11356-11364.
54. Loew, S.; Kooijman, E. E.; May, S., Increased pH-sensitivity of protein binding to lipid membranes through the electrostatic-hydrogen bond switch. *Chem Phys Lipids* **2013**, *169*, 9-18.
55. Sandoval, G., *Lipases and phospholipases : methods and protocols*. Humana Press: New York, 2012; p xv, 547 p.
56. Iwasaki, Y.; Nishikawa, S.; Tsuneda, M.; Takahashi, T.; Yamane, T., Detection of phospholipase D on solid materials. *Anal Biochem* **2004**, *329* (1), 157-159.
57. McDermott, M.; Wakelam, M. J. O.; Morris, A. J., Phospholipase D. *Biochem Cell Biol* **2004**, *82* (1), 225-253.
58. Brown, H. A., *Lipidomics and bioactive lipids : lipids and cell signaling*. Elsevier ; Academic Press: Amsterdam, Netherlands ; Boston San Diego, 2007; p xlvii, 342 p., 8 p. of plates.
59. Caroff, M.; Karibian, D., Structure of bacterial lipopolysaccharides. *Carbohydr Res* **2003**, *338* (23), 2431-2447.
60. Nikaido, H., Molecular basis of bacterial outer membrane permeability revisited. *Microbiol Mol Biol R* **2003**, *67* (4), 593-+.
61. Goto, S.; Sakai, S.; Kera, J.; Suma, Y.; Soma, G. I.; Takeuchi, S., Intradermal administration of lipopolysaccharide in treatment of human cancer. *Cancer Immunol Immun* **1996**, *42* (4), 255-261.
62. Coughlin, R. T.; Peterson, A. A.; Haug, A.; Pownall, H. J.; McGroarty, E. J., A Ph Titration Study on the Ionic Bridging within Lipopolysaccharide Aggregates. *Biochim Biophys Acta* **1985**, *821* (3), 404-412.
63. Brogden, K. A.; Cutlip, R. C.; Lehmkuhl, H. D., Complexing of Bacterial Lipopolysaccharide with Lung Surfactant. *Infect Immun* **1986**, *52* (3), 644-649.
64. Abraham, T.; Schooling, S. R.; Beveridge, T. J.; Katsaras, J., Monolayer Film Behavior of Lipopolysaccharide from *Pseudomonas aeruginosa* at the Air-Water Interface. *Biomacromolecules* **2008**, *9* (10), 2799-2804.
65. Canadas, O.; Keough, K. M. W.; Casals, C., Bacterial Lipopolysaccharide Promotes Destabilization of Lung Surfactant-Like Films. *Biophys J* **2011**, *100* (1), 108-116.

66. Bergstrand, A.; Svanberg, C.; Langton, M.; Nyden, M., Aggregation behavior and size of lipopolysaccharide from Escherichia coli O55 : B5. *Colloid Surface B* **2006**, *53* (1), 9-14.
67. Aurell, C. A.; Wistrom, A. O., Critical aggregation concentrations of gram-negative bacterial lipopolysaccharides (LPS). *Biochem Biophys Res Commun* **1998**, *253* (1), 119-123.
68. Langley, S.; Beveridge, T. J., Effect of O-side-chain-lipopolysaccharide chemistry on metal binding. *Appl Environ Microb* **1999**, *65* (2), 489-498.
69. Wu, M. C.; Heath, E. C., Isolation and Characterization of Lipopolysaccharide Protein from Escherichia-Coli. *P Natl Acad Sci USA* **1973**, *70* (9), 2572-2576.
70. Wilkinson, S. G., Bacterial lipopolysaccharides - Themes and variations. *Prog Lipid Res* **1996**, *35* (3), 283-343.
71. Jann, B.; Reske, K.; Jann, K., Heterogeneity of Lipopolysaccharides - Analysis of Polysaccharide Chain Lengths by Sodium Dodecylsulfate Polyacrylamide Gel-Electrophoresis. *Eur J Biochem* **1975**, *60* (1), 239-246.
72. Hua, W.; Verreault, D.; Adams, E. M.; Huang, Z. S.; Allen, H. C., Impact of Salt Purity on Interfacial Water Organization Revealed by Conventional and Heterodyne-Detected Vibrational Sum Frequency Generation Spectroscopy. *J Phys Chem C* **2013**, *117* (38), 19577-19585.
73. Finlayson, A. C., The Ph Range of the Mohr Titration for Chloride-Ion Can Be Usefully Extended to 4-10.5. *J Chem Educ* **1992**, *69* (7), 559-559.
74. Luckham, P.; Wood, J.; Froggatt, S.; Swart, R., A Comparison of Directly Measured Forces and Monolayer Behavior of Dipalmitoylphosphatidic Acid. *J Colloid Interf Sci* **1992**, *153* (2), 368-377.
75. Salay, L. C.; Ferreira, M.; Oliveira, O. N.; Nakaie, C. R.; Schreier, S., Headgroup specificity for the interaction of the antimicrobial peptide tritrpticin with phospholipid Langmuir monolayers. *Colloid Surface B* **2012**, *100*, 95-102.
76. McNamee, C. E.; Kappl, M.; Butt, H. J.; Ally, J.; Shigenobu, H.; Iwafuji, Y.; Higashitani, K.; Graf, K., Forces between a monolayer at an air/water interface and a particle in solution: influence of the sign of the surface charges and the subphase salt concentration. *Soft Matter* **2011**, *7* (21), 10182-10192.
77. Rudolphi-Skorska, E.; Zembala, M.; Filek, M., Mechanical and Electrokinetic Effects of Polyamines/Phospholipid Interactions in Model Membranes. *J Membrane Biol* **2014**, *247* (1), 81-92.
78. Yun, H.; Choi, Y. W.; Kim, N. J.; Sohn, D., Physicochemical properties of phosphatidylcholine (PC) monolayers with different alkyl chains, at the air/water interface. *B Korean Chem Soc* **2003**, *24* (3), 377-383.
79. Grigoriev, D.; Miller, R.; Wustneck, R.; Wustneck, N.; Pison, U.; Mohwald, H., A novel method to evaluate the phase transition thermodynamics of Langmuir monolayers. Application to DPPG monolayers affected by subphase composition. *J Phys Chem B* **2003**, *107* (51), 14283-14288.
80. Zakanda, F. N.; Nott, K.; Paquot, M.; Lelo, G. M.; Deleu, M., Penetration behaviour of alkylbetainate chlorides into lipid monolayers. *Colloid Surface B* **2011**, *86* (1), 176-180.
81. Minones, J.; Minones, J.; Rodriguez-Patino, J. M.; Conde, O.; Iribarnegaray, E., Miscibility of amphotericin B-dipalmitoyl phosphatidyl serine mixed monolayers spread on the air/water interface. *J Phys Chem B* **2003**, *107* (17), 4189-4195.
82. Minones, J.; Patino, J. M. R.; Minones, J.; Dynarowicz-Latka, P.; Carrera, C., Structural and topographical characteristics of dipalmitoyl phosphatidic acid in Langmuir monolayers. *J Colloid Interf Sci* **2002**, *249* (2), 388-397.
83. deMeijere, K.; Brezesinski, G.; Mohwald, H., Polyelectrolyte coupling to a charged lipid monolayer. *Macromolecules* **1997**, *30* (8), 2337-2342.

84. Boggs, J. M., Effect of Lipid Structural Modifications on Their Intermolecular Hydrogen-Bonding Interactions and Membrane Functions. *Biochem Cell Biol* **1986**, *64* (1), 50-57.
85. Abramson, M. B.; Wilson, C. E.; Gregor, H. P.; Katzman, R., Ionic Properties of Aqueous Dispersions of Phosphatidic Acid. *J Biol Chem* **1964**, *239* (12), 4066-&.
86. Patil, G. S.; Dorman, N. J.; Cornwell, D. G., Effects of Ionization and Counterion Binding on the Surface-Areas of Phosphatidic Acids in Monolayers. *J Lipid Res* **1979**, *20* (5), 663-668.
87. Fridlind, A. M.; Jacobson, M. Z., A study of gas-aerosol equilibrium and aerosol pH in the remote marine boundary layer during the First Aerosol Characterization Experiment (ACE 1). *J Geophys Res-Atmos* **2000**, *105* (D13), 17325-17340.
88. Casares, J. J. G.; Camacho, L.; Martin-Romero, M. T.; Cascales, J. J. L., Effect of Na⁺ and Ca²⁺ Ions on a Lipid Langmuir Monolayer: An Atomistic Description by Molecular Dynamics Simulations. *Chemphyschem* **2008**, *9* (17), 2538-2543.
89. Vacha, R.; Siu, S. W. I.; Petrov, M.; Bockmann, R. A.; Barucha-Kraszewska, J.; Jurkiewicz, P.; Hof, M.; Berkowitz, M. L.; Jungwirth, P., Effects of Alkali Cations and Halide Anions on the DOPC Lipid Membrane. *J Phys Chem A* **2009**, *113* (26), 7235-7243.
90. Cordomi, A.; Edholm, O.; Perez, J. J., Effect of Force Field Parameters on Sodium and Potassium Ion Binding to Dipalmitoyl Phosphatidylcholine Bilayers. *J Chem Theory Comput* **2009**, *5* (8), 2125-2134.
91. Gurtovenko, A. A.; Vattulainen, I., Effect of NaCl and KCl on phosphatidylcholine and phosphatidylethanolamine lipid membranes: Insight from atomic-scale simulations for understanding salt-induced effects in the plasma membrane. *J Phys Chem B* **2008**, *112* (7), 1953-1962.
92. Bockmann, R. A.; Hac, A.; Heimbürg, T.; Grubmüller, H., Effect of sodium chloride on a lipid bilayer. *Biophys J* **2003**, *85* (3), 1647-1655.
93. Mukhopadhyay, P.; Monticelli, L.; Tieleman, D. P., Molecular dynamics simulation of a palmitoyl-oleoyl phosphatidylserine bilayer with Na⁺ counterions and NaCl. *Biophys J* **2004**, *86* (3), 1601-1609.
94. Marcus, Y., Thermodynamics of Solvation of Ions .5. Gibbs Free-Energy of Hydration at 298.15-K. *J Chem Soc Faraday T* **1991**, *87* (18), 2995-2999.
95. Casillas-Ituarte, N. N.; Chen, X. K.; Castada, H.; Allen, H. C., Na⁺ and Ca²⁺ Effect on the Hydration and Orientation of the Phosphate Group of DPPC at Air-Water and Air-Hydrated Silica Interfaces. *J Phys Chem B* **2010**, *114* (29), 9485-9495.
96. Collins, K. D., Ion hydration: Implications for cellular function, polyelectrolytes, and protein crystallization. *Biophys Chem* **2006**, *119* (3), 271-281.
97. Jagoda-Cwiklik, B.; Vacha, R.; Lund, M.; Srebro, M.; Jungwirth, P., Ion pairing as a possible clue for discriminating between sodium and potassium in biological and other complex environments. *J Phys Chem B* **2007**, *111* (51), 14077-14079.
98. Batchelor, J. D.; Olteanu, A.; Tripathy, A.; Pielak, G. J., Impact of protein denaturants and stabilizers on water structure. *J Am Chem Soc* **2004**, *126* (7), 1958-1961.
99. Marcus, Y., Effect of Ions on the Structure of Water: Structure Making and Breaking. *Chem Rev* **2009**, *109* (3), 1346-1370.
100. Faraudo, J.; Travesset, A., Electrostatics of phosphatidic acid monolayers: Insights from computer simulations. *Colloid Surface A* **2007**, *300* (3), 287-292.
101. Sovago, M.; Wurpel, G. W. H.; Smits, M.; Müller, M.; Bonn, M., Calcium-induced phospholipid ordering depends on surface pressure. *J Am Chem Soc* **2007**, *129* (36), 11079-11084.
102. Faraudo, J.; Travesset, A., Phosphatidic acid domains in membranes: Effect of divalent counterions. *Biophys J* **2007**, *92* (8), 2806-2818.

103. Martin-Molina, A.; Rodriguez-Beas, C.; Faraudo, J., Effect of Calcium and Magnesium on Phosphatidylserine Membranes: Experiments and All-Atomic Simulations. *Biophys J* **2012**, *102* (9), 2095-2103.
104. Bockmann, R. A.; Grubmuller, H., Multistep binding of divalent cations to phospholipid bilayers: A molecular dynamics study. *Angew Chem Int Edit* **2004**, *43* (8), 1021-1024.